



**Universiteit
Leiden**
The Netherlands

Using functional genetic screens to understand and overcome PARP inhibitor resistance

Paes Lobo Lopes Dias, M.

Citation

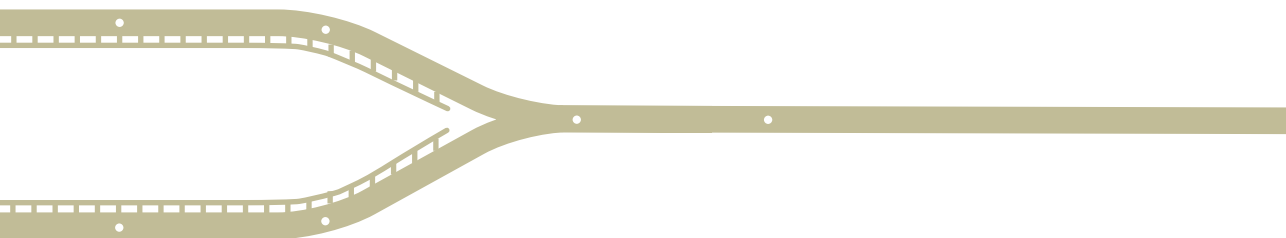
Paes Lobo Lopes Dias, M. (2023, January 18). *Using functional genetic screens to understand and overcome PARP inhibitor resistance*. Retrieved from <https://hdl.handle.net/1887/3512289>

Version: Publisher's Version

License: [Licence agreement concerning inclusion of doctoral thesis in the Institutional Repository of the University of Leiden](#)

Downloaded from: <https://hdl.handle.net/1887/3512289>

Note: To cite this publication please use the final published version (if applicable).



Chapter 5

Genome-wide dropout screens in BRCA1/53BP1 double-deficient cells as an approach to identify vulnerabilities of PARPi-resistant cells

Mariana Paes Dias, Ingrid van der Heijden, Cor Liefink, Anna Khalizieva, Yvette Faas, Carmen Fonseca, Jinhyuk Bhin, Justin Sprengers, Natalie Proost, Zuzanna Nowicka, Fendler Wojciech, Marieke van de Ven, Sven Rottenberg, Arnab Ray Chaudhuri, Roderick L. Beijersbergen, Piet Borst, and Jos Jonkers

In preparation

ABSTRACT

Tumors with loss of BRCA1 are defective for homologous recombination (HR) repair and hypersensitive to poly(ADP-ribose) polymerase inhibitors (PARPi). However, these tumors may acquire PARPi resistance via loss of DNA double-strand break (DSB) end-protection factors, such as 53BP1, which results in restoration of HR. In this chapter, we carried out a genome-wide functional genetic dropout screen in BRCA1/53BP1 double-deficient cells in order to identify vulnerabilities that could be exploited therapeutically to improve PARPi response. This screen yielded an extensive list of candidate genes, including thirteen subunits from mitochondrial complex I (MCI) as well as four genes associated with DNA damage response (DDR) pathways. Candidate genes with an $FDR \leq 0.3$ were selected for focused library screens in BRCA1-proficient and BRCA1/53BP1 double-deficient cells in order to validate our previous findings and to find genes whose loss augments the cytotoxicity of PARPi more strongly in BRCA1-deficient cells than in BRCA1-proficient cells. In these screens, we identified sixteen hits associated with DDR, including recombination and meiosis genes such as *SWSAP1* and *GGNBP2*, suggesting that rewiring of the DDR may revert PARPi resistance in BRCA1/53BP1 double-deficient cells. While individual validation of MCI subunits was technically hard to achieve, we found that loss of *SWSAP1* enhances toxicity of PARPi, *in vitro* and *in vivo*. Overall, in this chapter we show that genome-wide screens are a promising approach to identify candidate targets to improve PARPi response.

INTRODUCTION

Error-free repair of DNA double-strand breaks (DSBs) is achieved by homologous recombination (HR). BRCA1 and BRCA2 are key players in HR repair and heterozygous germline mutations in *BRCA1* or *BRCA2* genes predispose to breast and ovarian cancers that show HR deficiency due to loss of the wild-type *BRCA1/2* allele. The HR defect of *BRCA1/2*-mutated tumors can be targeted by the use of poly (ADP-ribose) polymerase (PARP) inhibitors (PARPi)^{1,2}.

PARP1, which is the main target of PARPi, is involved in various cellular processes, including the sensing of DNA single-strand breaks (SSBs). Upon damage, PARP1 is rapidly recruited to sites of DNA damage and transfers negatively charged ADP-ribose groups from donor NAD⁺ onto target proteins in a process termed poly(ADP-ribose)ylation (PARylation), required for SSB repair and thought to be inhibited upon PARPi treatment. PARP1 itself is a prime target of PARylation and the resulting PAR chains serve as a platform for the recruitment of downstream repair factors and subsequent release of PARP1 from the DNA, which is essential for repair to take place³. PARPi were initially thought to act by preventing the repair of SSBs, which accumulate during the S phase of the cell cycle, posing a threat to replication fork progression^{1,2}. This model was later challenged since PARPi were shown to trap PARP1 at DNA lesions due to impaired autoPARylation, resulting in DNA-protein crosslinks⁴⁻⁷. These crosslinks then trigger the collapse of replication forks that encounter trapped PARP1, leading to an accumulation of DSBs during S phase. Cells are dependent on BRCA1/2-mediated HR repair to resolve DSBs in an error-free manner and thus PARPi can induce DNA lesions that are lethal to BRCA1/2-deficient tumor cells but not to wild-type non-tumor cells.

The success of this approach has so far led to the approval of four different PARPi for the treatment of several cancers^{8,9}. However, while clinical trials have demonstrated promising response rates among patients receiving PARPi, most patients will inevitably develop resistance, resulting in disease relapse. Preclinical and clinical data have revealed that acquired resistance to PARPi can develop via three general mechanisms: (i) drug target-related mechanisms, such as upregulation of drug efflux pumps or mutations in PARP1 or functionally related proteins; (ii) restoration of HR via reactivation of BRCA1/2 or rewiring of the DDR network; (iii) restoration of replication fork stability⁸. Nonetheless, most of the mechanisms of PARPi resistance and resistance-associated factors identified thus far lead to the reactivation of the HR pathway. *In vitro* studies have shown that, in the impossibility of BRCA1/2 functional reactivation, HR can be restored in BRCA1-deficient cells through the loss of components of the 53BP1-RIF1-Shieldin complex¹⁰⁻¹⁸. There are two major forms of repair that cells employ to repair DSBs: non-homologous end joining (NHEJ) and HR. The choice between the two pathways is regulated in the context of the cell cycle. While NHEJ promotes the direct ligation of the broken DNA ends, and it is active throughout the cell cycle while favored in the G1 phase, HR is restricted to the S/G2 phase,

when the sister chromatid is available as a template for repair¹⁹. The 53BP1-RIF1-Shieldin complex plays a key role in NHEJ by suppressing DSB end-resection. In the absence of BRCA1/2, end-resection and consequently HR cannot take place in S/G2 phase and cells use error-prone NHEJ to repair DSBs. However, loss of any of the factors from the 53BP1-RIF1-Shieldin complex in BRCA1-deficient cells restores end-resection and HR, rendering these cells resistant to PARPi^{10–18}. Additional evidence that loss of the 53BP1-RIF1-shieldin end-protection pathway mediates resistance to PARPi comes from *in vivo* studies in mouse models of BRCA1-deficient breast cancer in which BRCA1 functional reactivation is not possible. These studies showed that acquired resistance, resulting from prolonged exposure of mice to PARPi, was frequently associated with HR restoration and loss-of-function alterations of *Trp53bp1* (ref. 20 and our own unpublished data). Moreover, loss of 53BP1 and shieldin components has been observed in patient-derived tumor xenograft (PDX) models with acquired resistance to PARPi, and mutations in *TP53BP1* have been reported in tumor biopsies from patients with metastatic BRCA1-associated breast cancer receiving platinum chemotherapy or PARPi^{18,21,22}.

In this study, we used functional genetic screens in BRCA1/53BP1 double-deficient cells to identify acquired vulnerabilities and modulators of PARPi response, which could potentially be targeted to improve PARPi response. This approach has previously yielded DNA ligase III (LIG3), a known DNA repair factor, as a collateral vulnerability of BRCA1-deficient cells with acquired PARPi resistance due to loss of DSB end-protection²³. While the previous screen used a DNA damage response (DDR)-focused library, in this study we carried out a genome-wide screen to expand our search beyond previously reported DNA damage repair factors. This genome-wide screen yielded an extensive list of candidate genes, which was used to generate a focused library for secondary screens in BRCA1/53BP1 double-deficient cells and BRCA1-proficient cells. We identified multiple candidate targets, including many subunits from the mitochondrial respiratory complex I (MCI). However individual validation of these subunits was technically hard to achieve. In addition, our screening efforts yielded several hits associated DNA damage response (DDR), including recombination and meiosis genes, such as *SWSAP1* and *GGNBP2*. While further investigation is required, our results suggest *SWSAP1* as a potential therapeutic target for the treatment of BRCA1/2-deficient cancers.

RESULTS

Genetic dropout screens in BRCA1/53BP1 double-deficient cells identify candidate modulators of PARPi resistance

To identify acquired vulnerabilities in BRCA1-deficient cells that developed PARPi resistance via BRCA1-independent restoration of HR, we carried out functional genetic dropout screens in *Brca1*^{-/-};*Trp53*^{-/-};*Trp53bp1*^{-/-} mouse embryonic stem (mES) cells (ES-B1P.R). Cells were transduced with a lentiviral genome-wide CRISPR library consisting of

90,230 single-guide RNAs (sgRNAs) targeting 18,424 genes (5 sgRNAs/gene) and were subsequently either mock-treated or treated for 3 weeks with 25 nM of the PARPi olaparib²⁴, which does not affect the viability of PARPi-resistant ES-B1P.R cells but is lethal to the corresponding PARPi-sensitive *Brca1*^{-/-};*Trp53*^{-/-} (ES-B1P.S) cells (**Fig. 1A**). Sequencing and analysis of the sgRNAs in the surviving cells yielded seventeen hits, including the Shu complex factors *Swsap1* and *Zswim7*, the base excision repair factor *Polb* and the transcription-coupled nucleotide excision repair factor *Cops7a*, as well as several subunits of the MCI, including *Ndufa8*, *Ndufs7*, *Ndufb8*, *Ndufa2*, *Ndufa1*, *Ndufa5*, *Ndufs8*, *Ndufa3*, *Ndufs1*, *Ndufb4*, *Ndufb10*, *Ndufb7* and *Nubpl* (**Fig. 1B,C**, **Supplementary Fig. 1A and Supplementary table 1**). Analysis of the predicted protein-protein interactions of all genes with a false discovery rate (FDR) ≤ 0.3 using the STRING database (<https://string-db.org/>) identified several gene clusters associated with mitochondrial oxidative metabolism such as complex I and Coenzyme Q (CoQ) of the mitochondrial respiratory chain, as well as lipoic acid metabolism (**Supplementary Fig. 1B**). STRING analysis also identified a cluster of diverse DDR factors and a cluster of genes associated with RNA-binding and processing of RNA secondary structures (**Supplementary Fig. 1B,C**).

To further validate our screening results, we carried out focused screens in BRCA1-deficient and BRCA1-proficient mouse and human cells, for which we generated custom mouse and human sgRNA libraries that included all candidate genes with FDR ≤ 0.3 (**Supplementary table 2**). We used BRCA1-deficient ES-B1P.R mES cells and isogenic BRCA1-proficient ES-P.R cells, as well as two isogenic human TERT-immortalized retinal pigment epithelial (RPE1) cell lines with engineered loss of TP53 (RPE1-P) or TP53+BRCA1+TP53BP1 (RPE1-B1P.R)¹⁶ (**Supplementary Fig. 2A**). The focused candidate screen in ES-B1P.R cells identified thirty-one genes, including eighteen genes associated with recombination-mediated repair (e.g., *Swsap1*, *Zswim7*, *Pds5b*, *Mnd1*, *Psmc3ip* (*Hop2*), *Rad18*, *Chd1l*, *Swi5*, *Chd1l*, *Rad54l*, *Hsf2bp*, *Rnf8*) and other repair pathways (e.g., *Cops7a*, *Usp22*, *Sp1*, *Cks1b*, *Cand1*, *Trip*) (**Fig. 1D**).

Screening in BRCA1-proficient cells allowed us to identify several hits that were specifically or stronger depleted in BRCA1-deficient cells (e.g., *Ggnbp2*, *Mnd1* and *Swsap1* in mES cells, and *HELQ* in RPE1 cells) (**Fig. 1E-I and Supplementary Fig. 2B**). Additionally, our screens identified genes whose loss was synthetic lethal in BRCA1/53BP1 double-deficient cells, but not in BRCA1-proficient cells, such as *Rnf8* in RPE1 cells (**Fig. H and Supplementary Fig. 2D-F**). The focused screen in RPE1-B1P.R cells yielded fewer hits than the focused screen in ES-B1P.R mES cells, which is expected as the focused library was based on the genome-wide screen results carried out in the same mES cells (**Fig. 1F,G**). Nonetheless, the screens in RPE1-B1P.R cells identified several genes previously reported to suppress response to PARPi, such as *RNASEH2A*²⁵, *ATM*^{10,13}, and *CHD1L/ALC1*²⁶⁻²⁹. These genes were also identified as hits in the mES screens, although their context specificity (i.e., specific to BRCA1-deficient cells) varied between the two cell lines (**Fig. 1D-I and Supplementary Fig. 2B,C**).

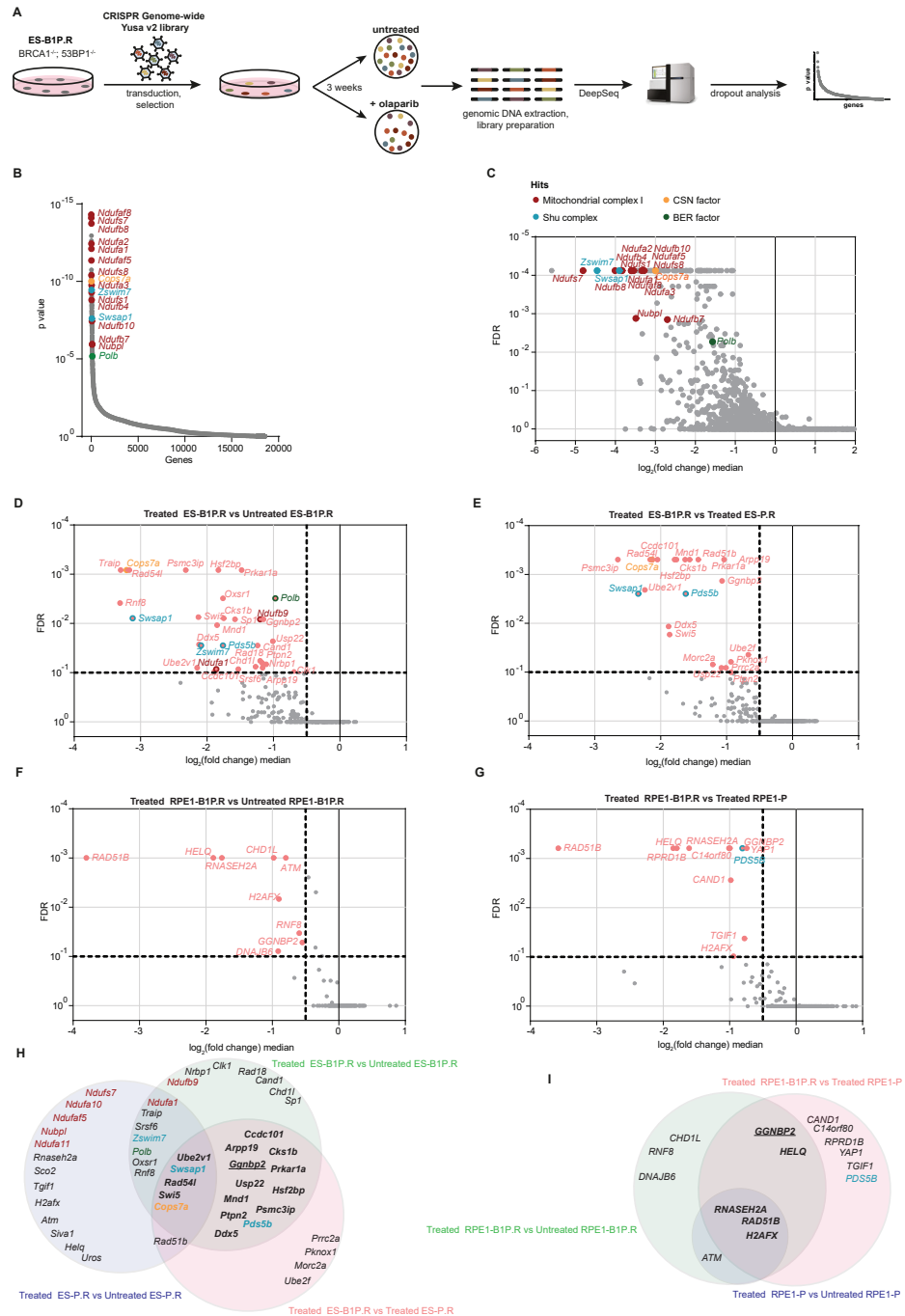


Figure 1 | Genetic dropout screens in BRCA1/53BP1 double-deficient cells identify candidate modulators of PARPi resistance. **A** | Outline of genome-wide dropout screen in ES-B1P.R cells, using mouse improved genome-wide knockout CRISPR library v2. Cells were treated with 25nM olaparib for three weeks or left untreated. **B** | Plot of distribution of the one-sided p value (gene dropout) for all genes targeted by the sgRNA library. **C** | Plot of distribution log₂ ratio (fold change (treated versus untreated)) median for all genes versus false

discovery rate (FDR) of results from genome-wide screen in ES-B1P.R cells. **D** | Plot of distribution \log_2 ratio (fold change (treated versus untreated)) median for all genes versus FDR of results from screen using focused candidate library in ES-B1P.R cells. **E** | Plot of distribution \log_2 ratio (fold change (treated ES-B1P.R versus treated ES-P.R)) median for all genes versus false FDR of results from screen using focused candidate library in mES cells. **F** | Plot of distribution \log_2 ratio (fold change (treated versus untreated)) median for all genes versus FDR of results from screen using focused candidate library in RPE1-B1P.R cells. **G** | Plot of distribution \log_2 ratio (fold change (treated RPE1-B1P.R versus treated RPE1-P)) median for all genes versus FDR of results from screen using focused candidate library in human RPE1 cells. **H** | Venn diagram depicting significant genes in mES and RPE1 screens.

Loss of GGNBP2 was the only common hit in both mES and RPE1 cells to increase PARPi sensitivity in BRCA1/53BP1 double-deficient cells but not in BRCA1-proficient cells (**Fig. 1D-J and Supplementary Fig. 2B,C**). GGNBP2 (a.k.a. LCRG1) plays a key role in spermatogenesis and one study reported GGNBP2 to be involved DSB repair during meiotic progression^{30,31}. Preliminary data showed that CRISPR-mediated deletion of GGNBP2 moderately increases response to olaparib treatment (**Supplementary Fig. 2G**). Of note, working antibodies against GGNBP2 were not available and quantification of gene expression by RT-PCR revealed residual mRNA expression, suggesting that GGNBP2 was not completely lost (**Supplementary Fig. 2H**). Analysis of whole-genome sequencing data of metastatic solid tumors from 16 patients who received PARPi (olaparib or niraparib) as single or combination therapy³² showed that patients with tumors with lower *GGNBP2* copy number responded better to the treatment, whereas patients with tumors with higher *GGNBP2* copy number status had progressive disease (**Supplementary Fig. 2I**). While these data are limited, they indicate that *GGNBP2* copy number might correlate with response to PARPi in patients. Further investigation is required to conclusively determine the effect of GGNBP2 in PARPi response. Altogether, the screens carried out in this study yielded a list of potential candidate targets to increase response to PARPi.

Validation of mitochondrial complex I subunits

As mentioned above, our initial genome-wide screen yielded several subunits of the MCI (**Fig. 1B,C and Supplementary Fig. 1B,C**). While only *Ndutf8*, *Ndufs7*, *Ndufb8*, *Ndutf2*, *Ndutf1*, *Ndutf5*, *Ndufs8*, *Ndutf3*, *Ndufs1*, *Ndufb4*, *Ndufb10*, *Ndufb7* and *Nubpl* scored as hits using the strict hit selection criteria, almost all of the MCI subunits encoded in the nuclear DNA scored as significant (\log_2 ratio (fold change (treated versus untreated)) median for all genes ≤ -1 ; FDR ≤ 0.1) (**Fig. 2A**). Given that MCI is responsible for oxidation of NADH to NAD⁺, these results suggest that a block in this process might sensitize the cells to PARPi (**Fig. 2B**).

We hypothesized that disruption of MCI leads to a strong increase in the cellular NADH/NAD ratio, resulting in decreased amounts of NAD⁺ available as substrate for PARP1. This might lead to decreased residual PARP1 activity in the presence of PARPi, and thus to increased PARPi-mediated toxicity. To test our hypothesis, we transduced ES-B1P.R cells with sgRNAs targeting two of the best scoring MCI genes in the initial genome-wide

screen, *Ndufa2* and *Ndufaf8* (**Fig. 1B, C**). TIDE analysis revealed a Cas9 cutting efficiency of around 60% for both genes³³. To assess functional impairment of MCI, we quantified mitochondrial oxygen consumption rate (OCR) measured with the Seahorse Bioanalyzer XFe24. Both, *Ndufa2*- and *Ndufaf8*-disrupted pools showed a decrease of around 50% in OCR, when compared to cells transduced with a non-targeting sgRNA (sgNTG), suggesting that deletion of *Ndufa2* and *Ndufaf8* impairs MCI (**Fig. 2C and Supplementary Fig. 3A**). Unfortunately, we were unable to obtain *Ndufa2* and *Ndufaf8* knockout (KO) clones, as these cells grew gradually slower after three to four weeks in culture. In addition, *Ndufa2* and *Ndufaf8* KO cells induced fast acidification of the cell culture medium. We therefore decided to use shRNA-mediated depletion to validate our initial screen in ES-B1P.R cells. Since shRNAs targeting NDUFAF8 were not available, we tested shRNA-mediated depletion of NDUFA2 and NDUFS8. shRNA-mediated depletion of both MCI factors in ES-B1P.R cells resulted in increased PARPi toxicity, albeit moderate in cells with shRNA-mediated depletion of NDUFA2. Moreover, shRNA-mediated depletion of NDUFS8 resulted in impaired growth in untreated conditions (**Fig. 2D**). Similar results were observed in mouse-tumor derived BRCA1/53BP1 double-deficient KB1P.R cells, derived from a *K14cre;Brca1^{F/F};Trp53^{F/F}* (KB1P) mouse mammary tumor that acquired resistance to PARPi *in vivo* because of loss of 53BP1 function^{20,23}. shRNA-mediated depletion of NDUFA2 and NDUFS8 in KB1P.R cells resulted in growth defects in untreated conditions, even though depletion of NDUFA2 did result in increased sensitivity to olaparib (**Fig. 2E**). Short-term cytotoxic assays in ES-B1P.R cells with shRNA-mediated depletion of NDUFA2 and NDUFS8 showed similar results as in long-term clonogenic assays, suggesting seeding cells at higher density does not improve growth of MCI-deficient cells (**Fig. 2F**).

In the initial genome-wide screen, we didn't observe decreased growth of MCI-depleted ES-B1P.R cells in untreated conditions, as sgRNAs targeting MCI subunits did not show a reduction in reads among the total cell population, compared to the day of seeding (i.e. starting day of the screen) (**Supplementary table 1**). However, validation experiments using sgRNAs and shRNAs suggested the opposite. We hypothesized that faster medium acidification might contribute to the reduced growth of MCI-deficient cells, and that in the context of the genome-wide screen, MCI-proficient cells could compensate for the very minor proportion of MCI-deficient cells. To test if co-culture with parental cells could rescue the growth defect of MCI-depleted ES-B1P.R cells, we decided to carry out competition assays in which parental and MCI-depleted cells were mixed in different ratios, followed by treatment with olaparib for two weeks. As control, we included a condition where we mixed PARPi-sensitive ES-B1P.S cells with ES-B1P.R cells (**Fig. 2G**). According to the initial genome-wide screen results, we should expect an enrichment of the GFP-labeled parental cells in olaparib-treated conditions, whereas in untreated conditions the ratio of parental to shRNA-depleted cells should remain constant. However, while we observed progressive loss of NDUFA2-deficient and NDUFS8-deficient ES-B1P.R cells with increasing PARPi concentrations, the initial cell ratio was not maintained in untreated conditions, suggesting

that the tested co-culture ratios contained insufficient MCI-proficient cells to suppress the growth defect of MCI-depleted cells (**Fig. 2G**). Of note, cells with shRNA-mediated depletion of *NDUFA2* showed only a mild growth defect and the ratios in untreated conditions were close to the ratios of the starting population, in line with the previous results (**Fig. 2D**). We next tested if chemical inhibition of MCI by rotenone, piericidin A or metformin could recapitulate the results observed in our initial screen. Treatment of ES-B1P.R cells with MCI inhibitors resulted in impaired growth and rapid medium acidification. Nevertheless, combined treatment with olaparib and MCI inhibitors tended to induced stronger growth inhibition than either of the single-agent treatments (**Fig. 2H-J**). Overall, we were unable to validate the results of our genome-wide screen and to conclusively establish that loss of MCI subunits increases response to PARPi.

Effect of pyruvate supplementation in MCI-deficient cells

Several studies have shown that supplementation with uridine and pyruvate/aspartate enables cells to grow without a functional respiratory chain^{25,34–36}. It has been suggested that glycolysis can provide sufficient ATP when the respiratory chain is compromised; however, NAD^+ regenerated during respiration is also required for production of aspartate via the malate-aspartate shuttle^{34,36}. In turn, aspartate is a key precursor for both purines and pyrimidines. Since aspartate levels in blood are low and most cells are unable to take up aspartate from the environment, respiratory chain-compromised cells need additional electron acceptors for carbon biosynthesis, such as aspartate and nucleotide base synthesis, to maintain proliferation^{34,36}. Indeed, it has been shown that the anti-proliferative effects of the MCI inhibitors metformin, rotenone and piericidin A can be suppressed by supplementation with pyruvate³⁵ (**Supplementary Fig. 3B**).

We therefore decided to test if supplementation with pyruvate would rescue the growth defects of our MCI-deficient cells. Preliminary data suggested that ES-B1P.R *Ndudaf8* KO cells require pyruvate for proliferation, as addition of pyruvate, alone or in combination with lactate, improved growth of these cells when compared with medium supplemented with lactate only (**Supplementary Fig. 3C,D**). Also, the growth defect of ES-B1P.R cells in which MCI was impaired via shRNA-mediated depletion of *NDUFA2* or *NDUFS8* could be rescued by supplementation with pyruvate (**Supplementary Fig. 3D**). The effect of pyruvate on the MCI-depleted cells was striking, as they seemed to proliferate even better than the parental cells with pyruvate supplementation, although *NDUFS8*-deficient cells seemed to reach a plateau earlier. On the contrary, supplementation with lactate did not improve proliferation of MCI-depleted cells and impaired proliferation of parental cells to levels comparable with MCI-depleted cells, suggesting that the proliferation defect in MCI-depleted cells is, at least in part, due to increased lactate levels, which would explain the rapid medium acidification. Further experiments will be required to confirm these preliminary data.

Figure 2

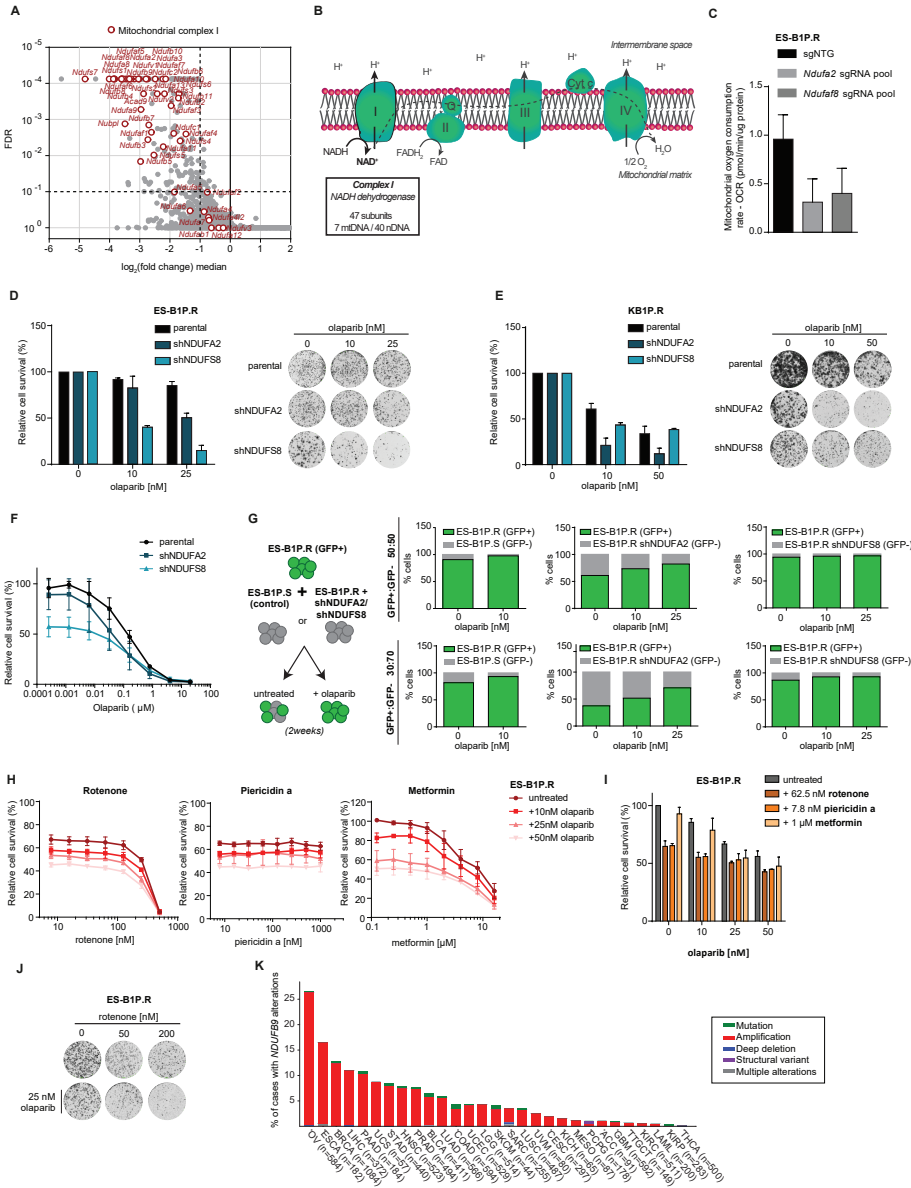


Figure 2 | Validation of mitochondrial complex I subunits. A | Plot of distribution \log_2 ratio (fold change) median (treated versus untreated) for all genes versus false discovery rate (FDR) of results from genome-wide screen in ES-B1P.R cells displaying all MCI genes included in the screen. **B** | Oxidative phosphorylation depicting complex I, II, III and IV. MCI is composed by 47 subunits, 7 encoded in mitochondrial DNA and 40 encoded in nuclear DNA, and is responsible for oxidation of mitochondrial NADH to NAD^+ . **C** | Quantification of mitochondrial oxygen consumption rate (OCR) measured with the Seahorse Bioanalyzer XFe24 in ES-B1P.R transduced with sgRNA non-targeting (sgNTG) or with sgRNA targeting the genes *Ndufa2* and *Ndufa8*. **D-E** | Quantification and representative images of long-term clonogenic assays in ES-B1P.R (D) and in KB1P.R (E) cell lines, treated with olaparib. Cells were treated for the whole extent of the assay. **F** | Quantification of short-term cytotoxicity assay in ES-B1P.R cells treated with olaparib. **G** | Competition assay with parental and MCI-deficient cells mixed in

different ratios (50:50% and 30:70%). ES-B1P.S were used as control. Cells were treatment with PARPi for 2 weeks and passaged twice a week. Measurement of GFP-positive cells was done by FACS. **H-I** | Quantification of short-term cytotoxicity assay in ES-B1P.R cells treated with olaparib in combination with the indicated MCI inhibitors. **J** | Representative images of long-term clonogenic assay in ES-B1P.R cells treated with olaparib and rotenone. **K** | An overview of the frequency of alterations of the *NDUFB9* gene across all available Cancer Genome Atlas (TCGA) PanCancer Atlas cohorts with at least one samples altered.

The MCI subunit *NDUFB9* is frequently amplified in human cancers

The focused candidate screen in ES-B1P.R cells failed to identify as many MCI subunits as in the original screen in the same cell line, with the exception of *Ndufa1* and *Ndufb9*. Moreover, sgRNAs targeting *Ndufa1*, *Ndufb9* and other MCI factors were depleted in untreated conditions, in line with our validation experiments but in contrast to the initial screen (**Supplementary Fig. 2D**). Notably, in the Cancer Genome Atlas (TCGA) PanCancer Atlas, containing over 10,000 primary tumors encompassing 33 different cancer types (www.cbioportal.org), *NDUFB9* was found amplified in several cancer types that are treated with PARPi, including ovarian cancer (27%), breast cancer (13%), pancreatic cancer (11%) and prostate cancer (8%) (**Fig. 2K**). *Ndufa1*, *Ndufs7*, *Ndufa10*, *Ndufaf5*, *Nubpl* and *Ndufa11* were also identified as hits in the BRCA1-proficient ES-P.R cells, suggesting that the increase in PARPi-mediated toxicity upon MCI impairment is BRCA1-independent. In line with this, shRNA-mediated depletion of *NDUFA2* and *NDUFS8* in BRCA1-proficient KP cells derived from a *K14cre;Trp53^{F/F}* (KP) mouse mammary tumor, increased response to olaparib (**Supplementary Fig. 2B,E and 3E**)³⁷. Of note, none of the MCI subunits scored as hits in the focused screens carried out in RPE1 cells. This could possibly be a result of differences in oxygen availability, since the screens in mES cells were carried out in normal oxygen conditions, while RPE1 cells were cultured in low oxygen (3%).

Validation of Shu complex factors

Our genome-wide dropout screen also identified two members of the Shu complex, *Swsap1* and *Zswim7* (a.k.a. *Sws1*) (**Fig. 1B,C and supplementary Fig. 1B**). The Shu complex is a recently identified complex that is critical for promoting the assembly of both RAD51 and its meiotic counterpart, DMC1, nucleoprotein filaments at resected DNA ends during meiotic HR^{38,39}. SWSAP1 was identified in human cells through its association with SWS1 and is considered to be a novel RAD51 paralog since, like RAD51 and the canonical RAD51 paralogs, it contains Walker A and B motifs predicted to be important for nucleotide binding/hydrolysis³⁹. Recent investigation of the human Shu complex revealed SPIDR and PDS5B as additional factors of the Shu complex^{40,41}. While *Pds5b* and *Spidr* did not score as hits with the strictest selection criteria in our genome-wide screen (**Supplementary Fig. 1A**), both genes had an FDR <0.3 and were therefore included in the focused library (**Supplementary Fig. 1B**).

In our focused library screen in ES-B1P.R cells, sgRNAs targeting *Swsap1* were found to be eight-fold depleted in olaparib-treated cells compared to untreated cells (**Fig. 1C,D**). sgRNAs targeting *Zswim7* and *Pds5b* were four-fold depleted in olaparib-treated cells

compared to untreated cells, whereas sgRNAs targeting *Spidr* were not significantly lost (**Fig. 1D**). *Swsap1* and *Zswim7* were also identified as hits our focused library screen in BRCA1-proficient ES-P.R cells, although depletion of *Swsap1*-targeting sgRNAs was four-fold stronger in PARPi-treated ES-B1P.R cells than in ES-P.R cells, suggesting that SWSAP1 loss augments the cytotoxicity of PARPi more strongly in ES-B1P.R cells than in ES-P.R cells (**Fig. 1E,H and supplementary Fig. 2B**). Interestingly, while most of the Shu complex factors did not score in RPE1 cells, shRNAs targeting *PDS5B* were significantly depleted in BRCA1-deficient RPE1-B1P.R compared to BRCA1-proficient RPE1-P cells (**Fig. 1F,G,I and supplementary Fig. 2C**).

Loss of SWSAP1 enhances *in vitro* efficacy of PARPi

Given the strong effect of SWSAP1 loss on PARPi-mediated toxicity in ES-B1P.R cells, we decided to investigate whether SWSAP1 would constitute a useful target for reversing PARPi resistance in BRCA1/53BP1 double-deficient cells. We therefore generated *Swsap1* KO clones in PARPi-resistant KB1P.R cells and in KB1P.S-53BP1KO cells, in which 53BP1 was deleted using CRISPR/Cas9. In line with our screening results, deletion of *Swsap1* rendered cells as responsive to olaparib as the PARPi-sensitive KB1P.S cells (**Fig. 3A,B and Supplementary Fig. 4A**). Loss of SWSAP1 also enhanced the toxicity of olaparib in PARPi-sensitive KB1P.S cells, suggesting enhanced response to PARPi mediated by SWSAP1 loss is not dependent on 53BP1 loss (**Fig. 3C and Supplementary Fig. 4A**). According to our screens, loss of SWSAP1 also increases PARPi response in BRCA1-proficient cells, albeit to a lesser extent than in BRCA1-deficient or BRCA1/53BP1 double-deficient cells. To test whether the effects of SWSAP1 loss on PARPi sensitivity are BRCA1-dependent, we used BRCA1-proficient KP cells and KB1P.S cells that were reconstituted with human BRCA1 (KB1P.S+hBRCA1). In both cell lines, *Swsap1* deletion increased olaparib-mediated toxicity in comparison to the non-modified cells, consistent with our screening results⁴² (**Fig. 3C and Supplementary Fig. 4A**). Of note, increased response of *Swsap1*-deleted KP cells to olaparib was only observed at much higher drug concentrations (above 1 μ M). Deletion of *Swsap1* in the mouse tumor cell lines also resulted in mild proliferation defects in untreated conditions (**Fig. 3A-D**). We next tested if deletion *SWSAP1* augments the response to PARPi in the isogenic RPE1-P and RPE1-B1P.R cell lines used for the focused candidate screens. Contrary to what was observed in the screen, deletion of *SWSAP1* enhanced response to olaparib in RPE1-B1P.R cells, although it also impaired proliferation (**Supplementary Fig. 4B**). Nonetheless, the proliferation defect observed upon deletion of *SWSAP1* was milder in RPE1-P cells, as well as the effect in PARPi-response (**Supplementary Fig. 4C**). Lastly, we investigated if deletion of *Swsap1* also increases PARPi response in BRCA2-deficient KB2P cells derived from a *K14cre;Brca2^{F/F};Trp53^{F/F}* (KB2P) mouse mammary tumor, as well as in BRCA2-reconstituted KB2P+hBRCA2 cells. While SWSAP1 loss had no effect on PARPi response in KB2P cells, we did observe an increased response to olaparib in

Swsap1-deleted KB2P+hBRCA2 cells, albeit milder than the increase observed in *Swsap1*-deleted KB1P.S+hBRCA1 cells (**Fig.3F,G**). Altogether, these results suggest that loss of SWSAP1 enhances PARPi response independently of BRCA1/2, although the strongest effect is observed in cells that originate from BRCA1-deficient tumors.

53BP1 loss and consequent restoration of HR activity has previously been shown to reduce the hypersensitivity of BRCA1-deficient cells to other DNA-damaging agents, such as topoisomerase I (TOP1) inhibitors²⁰. Hence, we decided to test if our *Swsap1*-deleted cells showed improved response to the TOP1 inhibitor camptothecin. Similar to olaparib, response to camptothecin was enhanced by SWSAP1 loss in all KB1P.R, KB1P.S and KB1P.S+hBRCA1 cell lines (**Fig. 3H,I**).

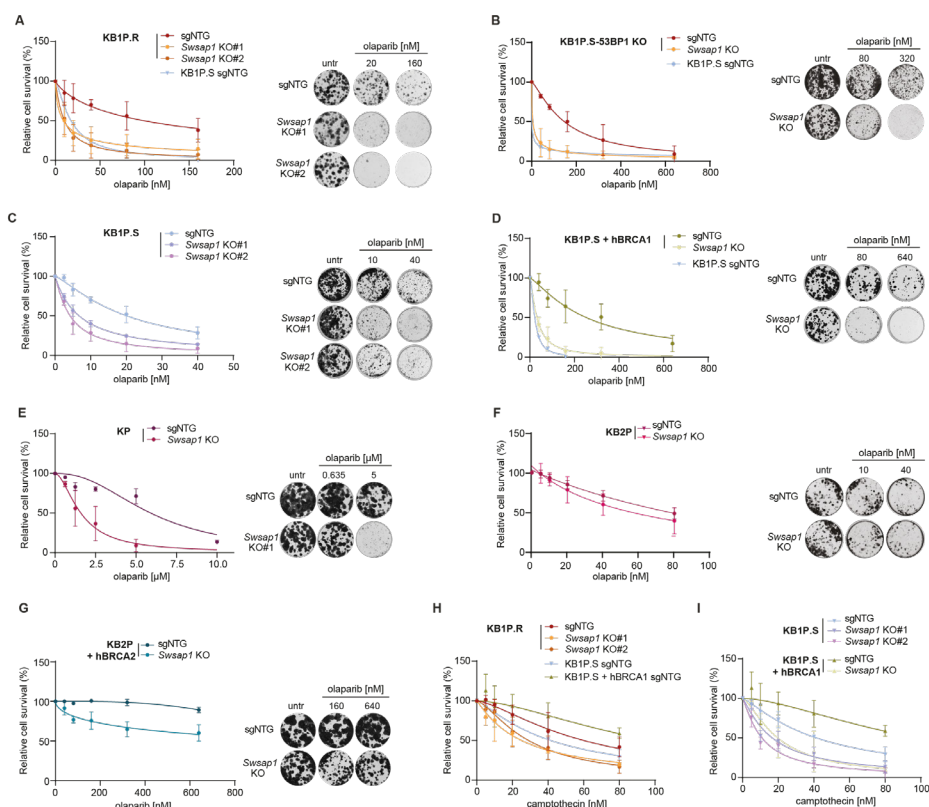


Figure 3 | Loss of SWSAP1 enhances in vitro efficacy of PARPi. A-F | Quantification and representative images of long-term clonogenic assays in KB1P.R (A), *Trp53bp1* deleted KB1P.S (KB1P.S-53BP1KO) (B), KB1P.S (C), KB1P.S reconstituted with human BRCA1 (KB1P.S+hBRCA1) (D), KP (E), KB2P (F) and KB2P reconstituted with human BRCA2 (KB2P+hBRCA2) (G) cell lines; treated with olaparib. Cells were treated for the whole extent of the assay. **H |** Quantification of long-term clonogenic assay in KB1P.R, KB1P.S and KB1P.S+hBRCA1 cell lines; treated with camptothecin for 6 hours the day after seeding. **I |** Quantification of long-term clonogenic assay in KB1P.S and KB1P.S+hBRCA1 cell lines, treated with camptothecin for 6 hours the day after seeding.

Effects of SWSAP1 loss on RAD51 loading and replication

We next tested if the *Swsap1*-deleted mouse mammary tumor cells displayed defective loading of RAD51, as previously suggested^{39–41}. To this end, we quantified the foci formation kinetics of RAD51 in KP cells exposed to ionizing radiation (IR) (10Gy), olaparib (500nM for 2 hours) or camptothecin (60nM for 4 hours). RAD51 foci formation was consistently delayed and reduced in *Swsap1*-deleted KP cells in response to all three damage-inducing agents (**Fig. 4A**). However, while loss of RAD51 loading could potentially explain increased response to PARPi in *Swsap1*-deleted KP, KB1P.S-53BP1KO and KB1P.S+hBRCA1 cells, it does not explain the increased response in KB1P.S cells, since these cells are already HR-deficient.

Several recent investigative advances have suggested that non-canonical RAD51 paralogs also play a role during DNA replication⁴³. We therefore measured replication fork progression in KB1P.S and KB1P.S+hBRCA1 cells in untreated conditions and observed that deletion of *Swsap1* resulted in longer tracks in KB1P.S but not in KB1P.S+hBRCA1 cells, suggesting that replication forks progressed faster in *Swsap1*-deleted BRCA1-deficient cells (**Fig. 4B,C**). We next looked at replication fork protection in the presence of hydroxyurea (HU), which results in replication stress by depleting the dNTP pool (**Fig. 4B**). In line with the known role of BRCA1 in replication fork protection, KB1P.S cells displayed shorter tracks in comparison to KB1P.S+hBRCA1; however, loss of SWSAP1 rescued fork protection in KB1P.S cells (**Fig. 4D**)⁴⁴. Since fork protection does not directly result in increased sensitivity to PARPi, but rather the opposite, suppression of fork degradation upon is not the reason for the increased sensitivity of SWSAP1-deficient cells to PARPi and topoisomerase II inhibitors. Further experiments will therefore be required to understand the mechanism(s) behind the increase drug sensitivity of *Swsap1*-deleted cells.

Loss of SWSAP1 enhances *in vivo* efficacy of PARPi in mice bearing BRCA1/2-deficient tumors

We next tested the effect of SWSAP1 loss *in vivo*. To this end, we orthotopically transplanted *Swsap1*-deleted KB1P.S and KB1P.S-53BP1KO cells, along with the corresponding non-modified lines, into the mammary fat pads of NMRI nude mice. Upon tumor outgrowth, mice were treated with olaparib or vehicle for 28 consecutive days, or with topotecan from days 0-14 and sacrificed when tumors progressed to a volume of 1,500 mm³. Olaparib-treated mice bearing *Swsap1*-deleted KB1P.S-53BP1KO tumors had increased survival compared with mice bearing unmodified PARPi-resistant KB1P.S-53BP1KO tumors (**Fig. 5A**). However, *Swsap1*-deleted tumors displayed slower growth and untreated mice had similar survival as the olaparib-treated ones, which challenges our *in vitro* observations (**Fig. 5A**). Also in PARPi-sensitive KB1P.S tumors, *Swsap1*-deletion further augmented the *in vivo* response to lower doses of olaparib, although the survival of some untreated mice bearing *Swsap1*-deleted KB1P.S tumors was similar to the survival of olaparib-treated mice due to slower growth of these tumors (**Fig. 5B**). Although the *in vivo* data do not exactly correlate

with what was observed *in vitro*, they suggest that SWSAP1 modulates growth of BRCA1-deficient tumors. Additional tumor intervention studies will be required to determine if loss of SWSAP1 improves the *in vivo* response of BRCA1/53BP1 double-deficient tumors to PARPi and if the slower growth and improved PARPi response of *Swsap1*-deleted tumors is independent of BRCA1 loss. Of note, mRNA expression of *Swsap1*, *Zswim7*, *Pds5b* and *Spidr* was significantly increased in KB1P and/or KB2P compared to KP tumors, suggesting that BRCA1/2-deficient tumors might display increased dependency on the Shu complex (Supplementary Fig. 4E-H).

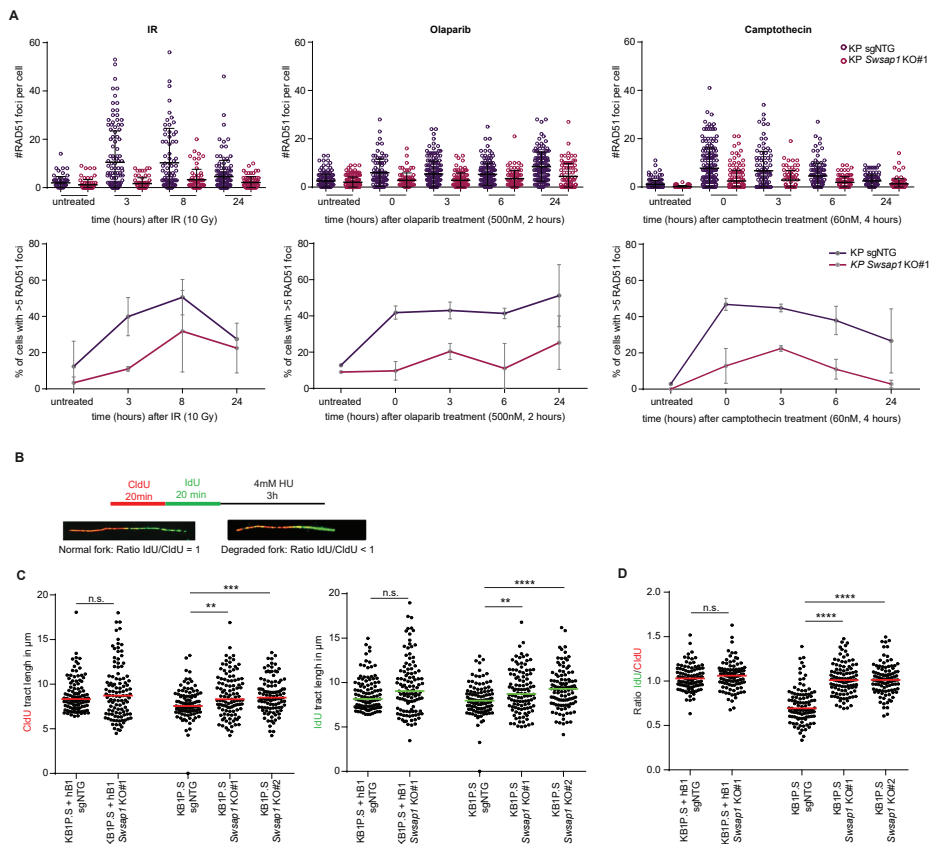


Figure 4 | Effects of SWSAP1 loss on RAD51 loading and replication. A | Quantification of RAD51 foci formation in KP cells, in response to ionizing radiation (IR) (10Gy), olaparib (500nM for 2 hours) and camptothecin (60nM for 4 hours), and following indicated recovery time. **B** | Experimental outline and representative images of normal and degraded replication forks. **C-D** | Quantification of fork progression (C) and fork degradation (D) in KB1P.S and KB1P.S+hBRCA1 cells. Data are represented as mean. ** $p < 0.01$, *** $p < 0.001$, **** $p < 0.0001$, n.s., not significant; Mann-Whitney U test.

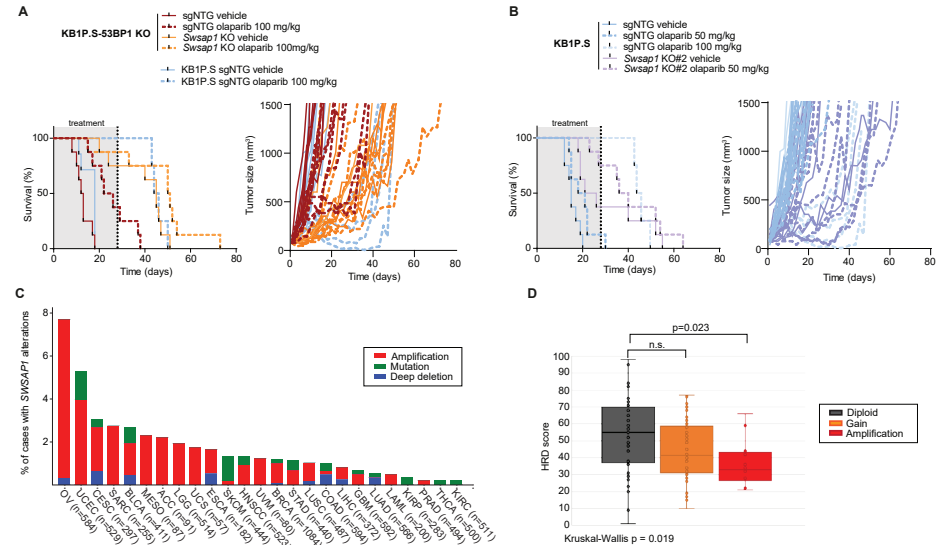


Figure 5 | Loss of SWSAP1 enhances in vivo efficacy of PARPi in mice bearing BRCA1/2-deficient tumors and SWSAP1 amplification is found in human cancers. **A** | Kaplan-Meier survival curves (left) and tumor growth curves (right) of mice transplanted with KB1P.S-53BP1 KO cells. Upon tumor outgrowth, mice were treated with 100 mg/kg olaparib for 28 days as is indicated by a dotted line. Curves corresponding to mice transplanted with KB1P.S cells are displayed as control. **B** | Kaplan-Meier survival curves (left) and tumor growth curves (right) of mice transplanted with KB1P.S cells. Upon tumor outgrowth, mice were treated with 50 mg/kg olaparib for 28 days as is indicated by a dotted line. Curves corresponding to mice transplanted with KB1P.S cells and treated with 100 mg/kg are displayed as control. **C** | An overview of the frequency of alterations of the *SWSAP1* gene across all available Cancer Genome Atlas (TCGA) PanCancer Atlas cohorts with at least one samples altered. **D** | Association between *SWSAP1* amplification and homologous recombination deficiency (HRD) score, which is the sum of scores for telomeric-allelic imbalance, large-scale transition, and loss-of-heterozygosity.

DISCUSSION

Molecular alterations that lead to resistance to targeted therapies often result in acquired vulnerabilities which could be exploited to design rational combination therapies and selectively kill unresponsive cancer cells. In this study, we carried out functional genetic loss-of-function screens in PARPi-resistant BRCA1/53BP1 double-deficient cells to identify specific dependencies of these cells that could be exploited to overcome PARPi resistance. In the initial genome-wide screen, we identified several hits associated with DDR and with oxidative phosphorylation, including multiple subunits of the MCI, whereas the hits from the follow-up focused screens were mostly associated with recombination-associated DNA repair. In line with this, we identified SWSAP1, part of the Shu complex and involved in meiotic recombination, as a modulator of PARPi response and show that loss of SWSAP1 enhances toxicity of PARPi, *in vitro* and *in vivo*. Altogether, this study generated an extensive list of potential modulators of PARPi response and shows that genome-wide functional genomic screens are a promising approach to identify candidate therapeutic targets to overcome resistance.

Mitochondrial Complex I

The MCI consists of forty-seven subunits, with forty of them encoded in the nuclear DNA. The genome-wide screen carried out in this study identified thirteen of these subunits as hits, and almost all were significantly depleted in olaparib-treated conditions ($\log_2FC \leq -1$; $FDR \leq 0.1$). However, validation of the effects of MCI loss on PARPi sensitivity proved difficult as cells didn't seem to tolerate MCI loss as well as in the initial screen. While most of our data are preliminary, our results indicate that modulation of PARPi response by MCI activity may be dependent on the tissue culture medium and on the surrounding cells/environment, suggesting that *in vitro* cultures may not be the best approach to validate our findings. Hence, one could envision experiments where the effect of shRNA-mediated depletion of MCI on PARPi response is tested *in vivo*, as previously described^{23,48}. In addition, as maintaining MCI-depleted cells over time proved to be technically difficult, it was not possible to test our hypothesis that MCI disruption results in a decrease in the NAD^+ available as substrate for PARP1, which in turn leads to decreased residual PARylation in the presence of PARPi, and consequently in increased PARP1 trapping and PARPi-mediated toxicity.

Nonetheless, the concept that residual PARylation levels modulate response to PARPi has already been suggested by previous work from our lab, which shows that PARG depletion and subsequent increase in PARylation leads to resistance to PARPi⁴⁶. Moreover, depletion of nicotinamide phosphoribosyltransferase (NAMPT), a rate-limiting enzyme in the NAD^+ salvage pathway, has been shown to enhance the cytotoxicity of PARPi in triple-negative breast cancer cells⁴⁹. Another study has suggested that increased levels of the NAD^+ derivative $NADP^+$ can act as endogenous PARPi by competing for the NAD^+ binding site of PARP1 and thereby suppressing PARylation. Consequently, cancer cells with high $NADP^+$ to NAD^+ ratios have increased sensitivity to PARPi, irrespective of their *BRCA1/2* mutation status, which might reflect reduced PARylation rather than PARP1 trapping onto DNA⁵⁰. Together with our preliminary data, these studies suggest that reduction of NAD^+ availability can impair PARylation which, in the presence of PARPi, can eliminate residual PARylation and enhance the toxicity of PARPi.

Oxidative metabolism has also been identified as a vulnerability of HR-deficient tumors. A recent study suggested that HR-deficient ovarian and breast cancers rely on oxidative metabolism to supply NAD^+ for PARP-dependent DNA repair mechanisms⁵¹. In addition, they show that metformin significantly affected PAR levels in both p53-deficient and *BRCA2/p53* double-deficient cells, although depletion was stronger in *BRCA2*-deficient cells. Surprisingly, combination of PARPi with MCI inhibitors impaired response to PARPi, contrary to our results. Further studies will be required to conclusively test if a block in the oxidation of NADH to NAD^+ eliminates residual PARylation and enhances PARPi response, and if it also affects other NAD^+ -using enzymes.

SWSAP1

RAD51 is crucial for HR and thus inhibiting alternative pathways of RAD51 loading might

sensitize cells to PARPi and help to combat resistance to PARPi. Our genome-wide and focused screens identified several members of the Shu complex as modulators of PARPi-mediated toxicity. *Swsap1* was the strongest hit from the Shu complex and further validation showed that deletion of *Swsap1* increases response to PARPi and topoisomerase II inhibitors, suggesting SWSAP1 could be a potential therapeutic target to improve drug response. Of note, the strongest effects of SWSAP1 loss on the response to PARPi (i.e., re-sensitization to drug doses similar or lower than KB1P.S cells) were observed in cells that originated from HR-deficient BRCA1-deficient tumors, even if HR had subsequently been restored via 53BP1 loss or BRCA1 re-expression (e.g., KB1P.R, KB1P.S-53BP1KO and KB1P.S+hBRCA1 cells). Weaker effects of SWSAP1 loss on PARPi response were observed in cells that always expressed wild-type BRCA1 (such as KP, KB2P+hBRCA2 and RPE1-p53-KO cells). Further validation in additional isogenic BRCA1/2-deficient and -proficient human cancer cell lines is required to understand if SWSAP1 is a specific vulnerability of BRCA1/2-deficient cells.

Additional evidence that SWSAP1 could be a potential therapeutic target in cancer therapy arises from the fact that survival data from genome-scale RNAi and CRISPR-Cas9 screens (<https://depmap.org/portal>) show that all four Shu complex factors (SWSAP1, ZSWIM7, PDS5B and SPIDR) are non-essential. Hence, toxicity associated with pharmacological inhibition of SWSAP1 in normal cells might be limited. In support of this, SWSAP1 is dispensable for mouse viability, albeit essential for male and female fertility^{38,41,52}. Similar knockout phenotypes were observed for ZWIM7 and SPIDR. In contrast, other RAD51 paralogs such as RAD51B, RAD51C, RAD51D, and XRCC2 are essential for embryonic survival.

To investigate if SWSAP1 might be a potential therapeutic target, we tested the effect of *Swsap1* deletion *in vivo* by orthotopically transplanting *Swsap1*-deleted KB1P.S and KB1P.S-53BP1KO cells into the mammary fat pad of NMRI nude mice. Deletion of *Swsap1* slowed tumor growth in untreated conditions in 6/8 KB1P.S-53BP1KO tumors and in 3/8 KB1P.S tumors, comparable to what was observed *in vitro*. Moreover, we observed an increased olaparib response in *Swsap1*-deleted KB1P.S tumors, but not in *Swsap1*-deleted BRCA1/53BP1 double-deficient tumors. The latter contrasts with the *in vitro* data and might be due to the slow growth of the *Swsap1*-deleted KB1P.S-53BP1KO tumors. Further *in vivo* studies are required to test the effect of prolonged olaparib treatment (e.g., 56 days instead of 28 days) on these tumors. Additionally, testing the effect of *Swsap1* deletion in BRCA1-proficient mammary tumors will be required to determine whether the impaired tumor growth and increased PARPi sensitivity caused by SWSAP1 loss are a specific vulnerability of BRCA1-deficient tumor cells.

Recent studies suggest the SWSAP1-ZSWIM7-SPIDR complex is critical for inter-homolog HR but dispensable for mitotic intra-chromosomal HR, explaining why patients and mice with loss-of-function mutations in this complex are viable⁴¹. In this study, we showed SWSAP1 is also important for the proliferation of BRCA1-deficient and BRCA1/53BP1

double-deficient tumor cells, and for their response to DNA damage-inducing agents like PARPi and topoisomerase II inhibitors. Similar to previous studies, we observed lower levels of DNA damage-induced nuclear RAD51 foci in *Swsap1*-deleted KP tumor cells, suggesting loss of Shu complex may impair HR repair in mitotic cells^{39–41}. Impaired HR could explain the increased sensitivity of *Swsap1*-deleted HR-proficient and HR-restored cells to PARPi and topoisomerase II inhibitors, but it does not explain the increased response of *Swsap1*-deleted HR-negative KB1P cells, suggesting that other mechanisms may underlie the effect of SWSAP1 loss on response to these DNA damage-inducing agents. Recent studies suggested non-canonical RAD51 paralogs also play a role during DNA replication stress and thus defects in replication stress response might explain the increased drug sensitivity of *Swsap1*-deleted HR-negative BRCA1/2-deficient cells⁴³. In line with this, KB1P.S cells showed faster replication fork progression, and replication fork protection was restored in KB1P.S cells. Fork protection reduces sensitivity to PARPi and thus suppression of fork degradation cannot explain the increased drug sensitivity of *Swsap1*-deleted cells. Additional experiments such as analysis of replication fork restart, fork asymmetry and induction of post-replicative single-stranded DNA (ssDNA) gaps will help understanding if replication stress is causal to the increased PARPi sensitivity of SWSAP1-deficient cells. Importantly, the Shu complex has also been reported to be important for the removal of alkylation adducts in ssDNA during replication and for the regulation of RAD52 localization during rDNA repair, and thus the role of these pathways in the response to PARPi should also be investigated^{43,54–56}.

Intriguingly, *SWSAP1* is frequently amplified in multiple cancer types (www.cbioportal.org), including ovarian cancer (7%) and breast cancer (1%), and ovarian cancers with amplified *SWSAP1* show lower HR-deficiency (HRD) scores. It would therefore be interesting to test if overexpression of SWSAP1 in BRCA1/2-deficient cells causes (partial) restoration of HR and RAD51 loading, and a reduced response to PARPi.

In sum, our screening efforts identified a comprehensive list of potential therapeutic targets that might be exploited to improve PARPi response. The majority of the hits arising from the secondary screens were associated with DDR and recombination, suggesting that rewiring of DDR is the most promising approach of reverting PARPi resistance in BRCA1/53BP1 double-deficient cells. However, screens in models which better represent physiological conditions (e.g., *in vivo* screens) will be important to determine if the non-DDR pathways identified by our screening efforts (e.g., oxidative phosphorylation) may also play a role in mediating PARPi resistance.

ACKNOWLEDGMENTS

We thank Peter Bouwman for sharing the mouse ES cells, Sylvie Noordermeer and Dan Durocher for the RPE1-TERT cells, and Roebi de Bruijn for the analysis of tumor RNA-seq. We thank Hanneke van der Gulden, the NKI Preclinical Intervention Unit, Digital Microscopy facility, Genomics Core facility and Animal facility for technical assistance. The underlying study have been made possible partly on the basis of the data that the Hartwig Medical Foundation (HMF, Utrecht, the Netherlands) and the Center of Personalized Cancer Treatment (CPCT, Rotterdam, the Netherlands). This work was supported by grants from the European Union Horizon 2020 research and innovation program (agreement 722729), Dutch Research Council (Vici 91814643, Vidi 193.131) and Onco Institute.

AUTHOR CONTRIBUTIONS

Conceptualization: M.P.D., P.B. and J.J.; Methodology: M.P.D., I.v.d.H., A.R.C and P.B.; Investigation: M.P.D., I.v.d.H., C.F., Y.F., A.K.; Animal studies: J.S., N.P., and M.v.d.V.; Data analysis: C.L., R.L.B. and J.B.; Writing of original draft, review & editing: M.P.D., P.B. and J.J.; Supervision: S.R., A.R.C and J.J.

METHODS

EXPERIMENTAL MODEL AND SUBJECT DETAILS

Cell Lines and cell culture

KP³⁷, KB1P.S, KB1P.R⁵⁷ and KB1P.S+hB1⁴² have been previously described.⁵³BP1KO KB1P.S cells as well as all *Swsap1* KO lines have been generated in this study. All these cell lines were cultured in DMEM/F12+GlutaMAX (Gibco) containing 5 µg/ml Insulin (Sigma), 5 ng/ml murine epidermal growth-factor (EGF, Sigma), 10% FBS and 50 units/ml penicillin-streptomycin (Gibco) and were cultured under low oxygen conditions (3% O₂, 5% CO₂ at 37°C). Mouse ES cells with a selectable conditional *Brca1* deletion (*R26Cre^{ERT2}/wt*; *Brca1^{SCo/-}*) have been previously described^{12,23}. These cells were cultured under normal oxygen conditions (21% O₂, 5% CO₂, 37°C), on gelatin-coated plates in 60% buffalo red liver (BRL) cell conditioned medium, 0.1 mM β-mercaptoethanol (Merck) and 10³ U/ml ESGRO LIF (Millipore) and 50 units/ml penicillin-streptomycin (Gibco); except when pyruvate supplementation was tested, for what we used DMEM+GlutaMAX without previous supplementation with pyruvate (GIBCO), supplemented with 10% FBS and 50 units/ml penicillin-streptomycin (Gibco). *Brca1* deletion in these cells was induced by incubation with 4-hydroxytamoxifen for three days. RPE1-hTERT cell lines were grown in DMEM+GlutaMAX (Gibco) supplemented with 10% FBS and 50 units/ml penicillin-streptomycin (Gibco),

under low oxygen conditions (3% O₂, 5% CO₂ at 37°C). RPE1-P, RPE1-B1P.S and RPE1-B1P.R cells were previously generated and the *SWSAP1* KO lines were established in this study¹⁶. HEK293FT (RRID: CVCL_6911) cells were cultured in IMDM+GlutaMAX-I (Gibco) supplemented with 10% FBS and 50 units/ml penicillin-streptomycin (Gibco), under normal oxygen conditions (21% O₂, 5% CO₂, 37°C).

Mice

All animal experiments were approved by the Animal Ethics Committee of The Netherlands Cancer Institute (Amsterdam, the Netherlands) and performed in accordance with the Dutch Act on Animal Experimentation (November 2014). Cell line transplantation experiments were performed in NMRI nude females, at the age of 6 weeks. NMRI nude animals were purchased from Janvier Labs. Animals were assigned randomly to the treatment groups and the treatments were supported by animal technicians who were blinded regarding the hypothesis of the treatment outcome.

METHOD DETAILS

Drugs

Olaparib (Syncom), camptothecin (Sigma), rotenone (Sigma) and piericidin a (Sandbio) were dissolved in DMSO. Metformin hydrochloride (Sigma) was dissolved in water. All dissolved compounds were stored at -20°C.

Functional Genetic Screens

Genome-wide screen

Mouse improved genome-wide knockout CRISPR library v2 was stably introduced into *Brca1*^{-/-}; *Trp53*^{-/-}; *Trp53bp1*^{-/-} mESCs by lentiviral transduction using a multiplicity of transduction (MOI) of 0.3, in order to ensure that each cell only gets incorporated with one only sgRNA. mES cells and organoids were selected with puromycin, 3 µg/ml, for 3 days and then seeded in the presence of 25nM olaparib, left untreated or pelleted for the genomic DNA isolation (T0). The total number of cells used in a single replicate was calculated as following: library complexity x coverage (500x). Cells were seeded at a density of 2.5 million cells per 15 cm dish and were kept in culture for 3 weeks and passaged every 7 days (and seeded in single cells) while keeping the coverage at every passage. Triplicates were performed for each condition. In the end of the screen, cells were pooled and genomic DNA was extracted (QIAmp DNA Mini Kit, Qiagen). sgRNA sequences were retrieved by a two-step PCR amplification, as described before⁴⁸. To maintain screening coverage, the amount of genomic DNA used as an input for the first PCR reaction was taken into account (6 µg of genomic DNA per 10⁶ genomes, 1 µg/PCR reaction). Resulting PCR products were purified using MiniElute PCR Purification Kit (Qiagen) and submitted for Illumina sequencing. Sequence alignment and dropout analysis was carried out using the algorithms MAGeCK (Li et al., 2014) and DESeq2^{58,59}. Gene ranking is generated automatically with MaGECK

algorithm. To generate gene ranking based on DESeq2 algorithm, we calculated per gene the number of hit sgRNAs and the mean of the \log_2 FoldChange over those sgRNAs. We then ranked the genes based on these two metrics.

Focused screen

For the design of the custom sgRNA library the BROAD GPP sgRNA design portal (<https://portals.broadinstitute.org/gppx/crispick/public>) was used. The sgRNA sequences targeting the candidate genes (**Supplementary table 2**), essential, non-essential, safe-haven regions (non-coding) and non-targeting genes were ordered as pool of oligonucleotides (TWIST Biosciences) with flanking sequences to enable PCR amplification and Gibson assembly into pLentiGuide-Puro (pLG, addgene #52963). The sgRNA library was generated as described previously, with modifications⁶⁰. The oligo library was amplified with KAPA® HiFi HotStart Polymerase (Roche, Catalog #KK2502) according to manufacturer protocol using 1x KAPA HiFi Fidelity buffer, 0.3mM each dNTP, 0.4 ng/ul oligo pool, 0.3uM pLG_U6_forward (5'- GGCTTTATATATCTTGTGGAAAGGACGAAACACCG-3'), 0.3uM pLG-TRACR_Reverse (5'-GACTAGCCTTATTTAACTTGCTATTTCTAGCTCTAAAAC-3'), 0.5 U KAPA HiFi HotStart DNA polymerase in a total volume of 25ul with the PCR conditions: 98°C, 3 min; denature 98°C, 30 sec; anneal 62°C, 15 sec; extend 72 °C 10, sec; 15 cycles followed by 10 min at 72°C. Purification of the PCR product was performed with the Isolate II PCR and Gel kit (Bioline, cat. BIO-52060) according to the manufacturer's directions. The linearized pLentiGuide plasmid backbone was extracted from gel using the Isolate II PCR and Gel kit (Bioline, cat no. BIO-52060) according to the manufacturer's directions. For Gibson assembly, each reaction contained 100ng purified digested plasmid and 5ng purified PCR product. The Gibson reaction were precipitated as as described previously and 100ng of the pooled sgRNA library was transformed in 25ul Endura Electrocompetent cells according to the manufacturer's instructions⁶⁰. After transformation and overnight colony growth, bacteria were collected by scraping in LB and plasmid DNA was isolated using Nucleobond Xtra Midi (Macherey-Nagel cat#740410). The representation of the sgRNA library was verified by next generation sequencing. Focused candidate screens were carried out similarly to genome-wide screen: ES-B1P.R cells were treated with 25nM olaparib for two weeks or left untreated; RPE1-P and RPE1-B1P.R were treated with 100nM olaparib for two weeks or left untreated. Triplicates were performed for each condition. DNA extraction and library preparation was carried out as in genome-wide screen.

Oxygen consumption rate (OCR)

OCR was measured using Seahorse Bioscience XFe24 Analyzer (Agilent). Cells were seeded 24hr before the assay in XF24 Seahorse Cell Culture microplates (Agilent) (sgNTG, 90,000 cells/well; sgNDUFA2, 100,000 cells/well; sgNDUFAF8, 120,000 cells/well). For OCR measurements, the following reagents were added: oligomycin (1 μ M), FCCP (0.4 μ M), and rotenone (1 μ M) and antimycin A (1 μ M). All results were normalized to protein content.

Briefly, cells were washed with PBS and then lyzed with RIPA buffer for 20 min. The protein concentration was then determined using Pierce BCA Protein Assay Kit (Thermo Scientific).

Long-Term Clonogenic Assays

Long-term clonogenic assays were performed in 6-well plates for the validation of MCI and in 12-well plates for validation of the Shu complex. Cells were seeded at low density to avoid contact inhibition between the clones (6-well: ES-B1P.R, 3,000 cells/well; KB1P.R, 2,500 cells/well; KP, 1,000 cells/well; 12-well: KB1P.S, 2,000 cells/well; KB1P.R, 1,000 cells/well; KB1P.S-53BP1KO, 1,000 cells/well; KB1P.S+hBRCA1, 500 cells/well; KB2P, 2,000 cells/well; KB2P+hBRCA2, 500 cells/well; KP, 500 cells/well; RPE1-P, 800 cells/well, RPE1-B1P.R, 1,000 cells/well) and cultured for 7-10 days. For the quantification of Shu complex experiments, cells were incubated with Cell-Titer Blue (Promega) reagent to measure cell viability and later fixed with 4% formaldehyde and stained with 0.1% crystal violet to generate representative images of the experiment. Because Cell-Titer Blue assay relies on cellular metabolic capacity, we decided not to use this tool to measure cell viability in the MCI experiments. Hence, at the end of the assay, cells were directly fixed with 4% formaldehyde and stained with 0.1% crystal violet and quantification was carried out by diluting (extraction) crystal violet with 1% acetic acid and absorbance was measured at 590 nm wavelength.

Short-term Cytotoxicity Assays

Cells were seeded in 96-well plates (parental and NDUFA2-depleted cells, 1,000 cells/well; NDUFS8-depleted cells, 2,000 cells/well) and the indicated drugs were added the next day and left for three days. At the end of the assay, plates were fixed with cold TCA (50 %) and left in the fridge for one hour, washed with water five times, and then airdried. For quantification, Sulforhodamine B (SRB) was added for 30 min. Plates were then washed three times with 1% acetic acid and left to airdry. 10mM TRIS solution was added to the dry plates for a short period to dissolve the SRB and absorbance was measured at 540 nm wavelength.

Competition assays

GFP-labeled parental cells and MCI-depleted cells were mixed at the indicated different ratios and treatment with olaparib for two weeks. At the end of the assay, cells were collected and FACS was performed using the BD LSRFortessa Cell Analyzer (BD Biosciences) equipped with the BD FACSDiva Software (v.8.0.2, BD Biosciences). Data were analyzed using FlowJo (v.10.7.1, BD Biosciences).

Proliferation assay

Cells were seeded at low density in 96-well plates (4,000 cells/well) and imaged every 4h using IncuCyte®, for 1 week duration. Cells were grown under normal oxygen conditions (21% O₂, 5% CO₂, 37°C), in the presence or absence of 1 mM pyruvate or 1 mM lactate.

Data was analyzed using IncuCyte ZOOM 2018A software.

Western Blot

Cells were trypsinized and then lysed in RIPA buffer for 20 min. The protein concentration was determined using Pierce BCA Protein Assay Kit (Thermo Scientific). SDS-Page was carried out with the Invitrogen NuPAGE SDS-PAGE Gel System (Thermo Fisher 4–12% Bis-Tris gels were used) buffer: MOPS; input: 40µg protein, according to the manufacturer's protocol. Next, proteins were electrophoretically transferred to a nitrocellulose membrane (Biorad). Before blocking, membranes were stained with Ponceau S, followed by blocking in 5% (w/v) milk in TBS-T for 1hr at RT. Membranes were incubated with primary antibody 4hrs at RT in 1% (w/v) milk in TBS-T (rabbit anti-SWSAP1, 1:500, antibody produced for this study). Horseradish peroxidase (HRP)-con-jugated secondary antibody incubation was performed for 1 hr at RT (anti-rabbit HRP 1:2000) in 1% (w/v) milk in TBS-T. Signals were visualized by ECL (Pierce ECL Western Blotting Substrate, Thermo Scientific).

RT-qPCR

In order to determine gene expression levels, RNA was extracted from cultured cells using ISOLATE II RNA Mini Kit (Bioline) and used as a template to generate cDNA with Tetro cDNA Synthesis Kit (Bioline). Quantitative RT-PCR was performed using SensiMix SYBR Low-ROX Kit (Bioline; annealing temperature – 60°C). *Swsap1_forward* (5'- GCTCCAGAAGGTTCTGTTTCCA -3'), *Swsap1_reverse* (5'- TCCAGAAGCAATGCAGCCAA -3'), *Ggnbp2_forward* (5'- GAG-GAGTTCCCCTTCGAGAG -3'), *Ggnbp2_reverse* (5'- GCACCATTATTCTGATGCCCAT -3').

RAD51 Foci Immunofluorescence

Cells were seeded on coverslips 24 hr prior the assay to achieve ~90% confluency. Cells were then EITHER irradiated using the Gammacell 40 Extractor (Best Theratronics Ltd.) at the dose of 10 Gy, treated with 500nM olaparib for 2 hr, or TREATED with 60nM camptothecin for 4 hr, and allowed to recover for the indicated times. Cells washed with PBS++ (PBS solution containing 1 mM CaCl₂ and 0.5 mM MgCl₂) and pre-extracted with 0.5% (v/v) Triton X-100 in PBS++ for 5 min. Next, cells were washed with PBS++ and fixed with 2% (v/v) paraformaldehyde solution in PBS for 20 min. cells were then permeabilized with ice-cold methanol/acetone solution (1:1) for 15 min. To minimize the background, cells were further incubated for 20 min in staining buffer (1% (w/v) BSA, 1% (v/v) FBS, 0.15% (w/v) glycine and 0.1% (v/v) Triton X-100 in PBS). Staining buffer was also used as a solvent for antibodies – primary antibody rabbit anti-RAD51, 1:1000, #70-002, Bioacademia; secondary antibody Alexa Fluor® 658-conjugated, 1:1000, A11011, Invitrogen. Incubation with primary and secondary antibodies was done for 2 hr and 1 hr, respectively. All incubations were performed at room temperature. Samples were mounted with VECTASHIELD Hard Set Mounting Media with DAPI (#H-1500; Vector Laboratories). Images were captured with Leica SP5 (Leica Microsystems) confocal system and analyzed using an in-house developed macro to

automatically and objectively evaluate the DNA damage-induced foci ¹⁰.

DNA Fiber Assay

DNA fiber analysis was conducted in accordance with the previously described protocol⁶¹. Cells were sequentially pulse-labelled with nucleotide analogues, 30µM CldU (c6891, Sigma-Aldrich) and 250µM IdU (I0050000, European Pharmacopoeia) for 20 min. After double labelling, cells were washed with PBS and either treated with 4mM HU for 3 hr or left untreated. Then, cells were harvested and resuspended in ice cold PBS to the final concentration 2.5 × 10⁵ cells per ml. Labelled cells were mixed with unlabeled cells at 1:1 (v/v), and 2.5 µl of cell suspension was spotted at the end of the microscope slide. 8 µl of lysis buffer (200mM Tris-HCl, pH 7.5, 50mM EDTA, and 0.5% (w/v) SDS) was applied on the top of the cell suspension, then mixed by gently stirring with the pipette tip and incubated for 8 min. Following cell lysis, slides were tilted to 15–45° to allow the DNA fibers spreading along the slide, air dried, fixed in 3:1 methanol/acetic acid overnight at 4 °C. Subsequently, fibers were denatured with 2.5 M HCl for 1 hr. After denaturation, slides were washed with PBS and blocked in blocking solution (0.2% Tween 20 in 1% BSA/PBS) for 40 min. After blocking, primary antibody solutions are applied, anti-BrdU antibody recognizing CldU (1:500, ab6326; Abcam) and IdU (1:100, B44, 347580; BD) for 2 hours in the dark at RT followed by 1h incubation with secondary antibodies: anti-mouse Alexa Fluor 488 (1:300, A11001, Invitrogen) and anti-rat Cy3 (1:150, 712-166-153, Jackson Immuno-Research Laboratories, Inc.). Finally, slides are washed with PBS and subsequently mounting medium is spotted and coverslips are applied by gently pressing down. Slides were sealed with nail polish and air dried. Fibers were visualized and imaged by Carl Zeiss Axio Imager D2 microscope using 63X Plan Apo1.4 NA oil immersion objective. Data analysis was carried out with ImageJ software⁶⁴.

In vivo Studies

Mouse tumor-derived cells were dissociated into single cells and collected in medium, filtered with 70µm nylon filters (Corning) and resuspended in complete media/BME mixture (1:1). All cell line suspensions contained a total of 500.000 cells per 40 µl of media/BME mixture, and were injected in the fourth right mammary fat pad of wild-type mice. Mammary tumor size was determined by caliper measurements (length and width in millimeters), and tumor volume (in mm³) was calculated by using the following formula: 0.5 × length × width². Upon tumor outgrowth to approximately 75 mm³, mice were treated with either vehicle or olaparib for 28 consecutive days. Animals were sacrificed with CO₂ when the tumor volume reached 1,500 mm³.

Correlation between GGNBP2 Copy Number Status and PARPi Response in HMF Cohort

Processed whole genome sequencing data on metastatic solid tumors were obtained from the Hartwig Medical Foundation (HMF) (data access request DR-184) and analyzed

based on their bioinformatic pipeline (<https://github.com/hartwigmedical/pipeline>) designed to detect all types of somatic alterations including structural variations and copy number aberrations as previously described⁶². Patients who received olaparib or niraparib as single or combination therapy were used to investigate the association between GGNBP2 copy number status and clinical response to PARP inhibitors. First RECIST response evaluated 8-12 weeks after the treatment was used to define clinical response.

TCGA Data Analysis and Comparison of HRD Score between Samples with SWSAP1 Gain/ Amplification and Samples with Wild-type (diploid) SWSAP1

Genomic data of OV cohort generated by The Cancer Genome Atlas (TCGA) consortium. Copy number and gene expression (as z-scores relative to all samples) data were downloaded from cBioPortal (<http://www.cbioportal.org/>) on 22 June 2022. Scores for telomeric-allelic imbalance (TAI), large-scale transition (LST), loss-of-heterozygosity (HRD LOH) and Homologous Recombination Deficiency (HRD) were downloaded from TCGA DDR Data Resources available under <https://gdc.cancer.gov/about-data/publications/PanCan-DDR-2018>. TAI represents the number of subchromosomal regions with allelic imbalance extending to the telomere, LST is the number of chromosomal breaks between adjacent regions of at least 10Mb, HRD LOH is the number of loss-of-heterozygosity regions of intermediate size (< 15Mb but < whole chromosome in length) and HRD Score is calculated from the three scores (TAI + LST + HRD LOH). HRD score and its components were compared between samples with different SWSAP1 copy number using Kruskal-Wallis test (global test) and post-hoc comparisons were made based on multiple comparisons of mean ranks of all group pairs (Siegel, Castellan, 1988, p. 213-215).

DATA AND SOFTWARE AVAILABILITY

Sequencing of all functional genetic screens was performed at the Netherlands Cancer Institute and results will be made available upon request. WGS data from HMF can be obtained through standardized procedures and request forms at <https://www.hartwigmedicalfoundation.nl>. The TCGA ovarian cancer dataset used in this study is available with informed consent under the authorization of local Institutional Review Boards (<https://www.cancer.gov/about-nci/organization/ccg/research/structural-genomics/tcga>). Copy number data used for this manuscript are deposited by the GDC (<https://gdc.cancer.gov/about-data/publications/pancanatlas>).

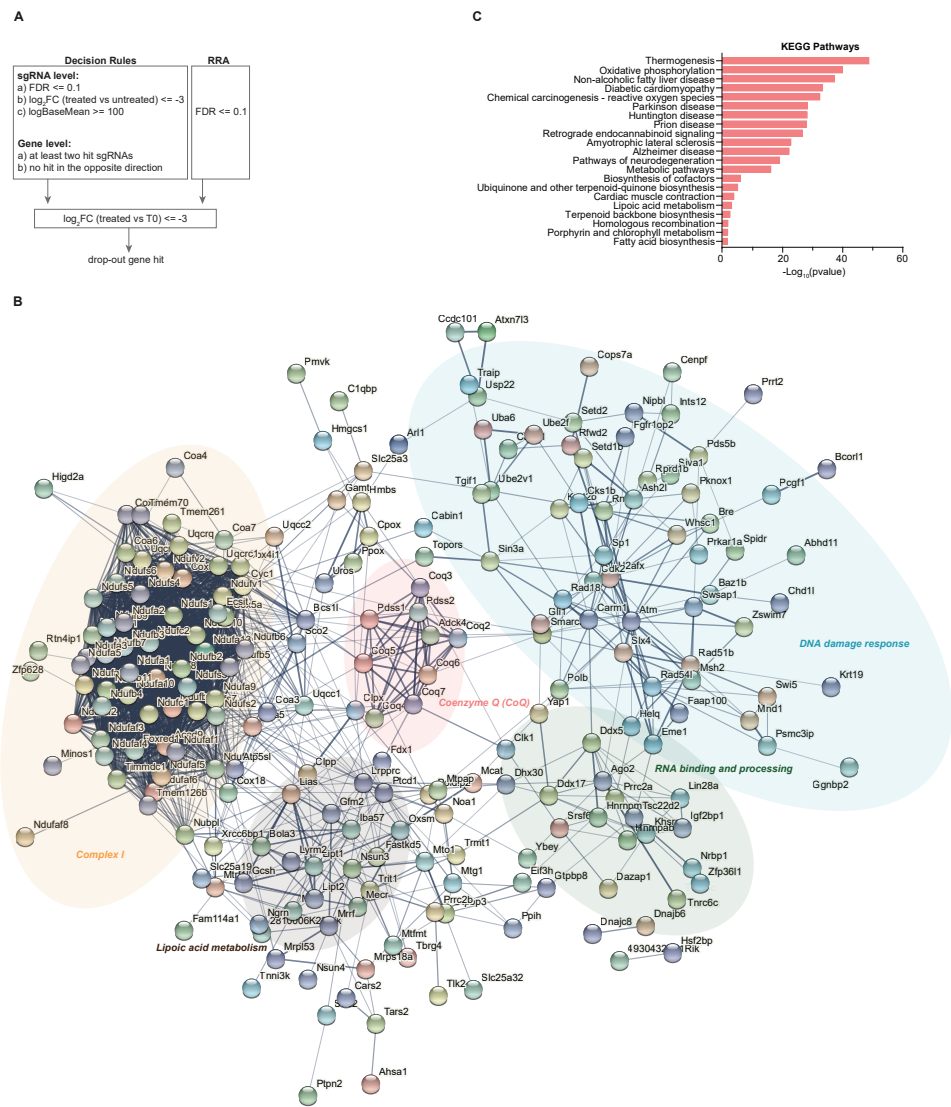
REFERENCES

1. Farmer, H. *et al.* Targeting the DNA repair defect in BRCA mutant cells as a therapeutic strategy. *Nature* **434**, 917–21 (2005).
2. Bryant, H. E. *et al.* Specific killing of BRCA2-deficient tumours with inhibitors of poly(ADP-ribose) polymerase. *Nature* **434**, 913–917 (2005).
3. Pascal, J. M. & Ellenberger, T. The rise and fall of poly(ADP-ribose): An enzymatic perspective. *DNA Repair (Amst)*. **32**, 10–16 (2015).
4. Helleday, T. The underlying mechanism for the PARP and BRCA synthetic lethality: Clearing up the misunderstandings. *Molecular Oncology* **5**, 387–393 (2011).
5. Ström, C. E. *et al.* Poly (ADP-ribose) polymerase (PARP) is not involved in base excision repair but PARP inhibition traps a single-strand intermediate. *Nucleic Acids Res.* **39**, 3166–3175 (2011).
6. Murai, J. *et al.* Trapping of PARP1 and PARP2 by clinical PARP inhibitors. *Cancer Res.* **72**, 5588–5599 (2012).
7. Murai, J. *et al.* Stereospecific PARP trapping by BMN 673 and comparison with olaparib and rucaparib. *Mol. Cancer Ther.* **13**, 433–443 (2014).
8. Paes Dias, M., Moser, S. C., Ganesan, S. & Jonkers, J. Understanding and overcoming resistance to PARP inhibitors in cancer therapy. *Nature Reviews Clinical Oncology* 1–19 (2021). doi:10.1038/s41571-021-00532-x
9. Mateo, J. *et al.* A decade of clinical development of PARP inhibitors in perspective. *Ann. Oncol.* **30**, 1437–1447 (2019).
10. Xu, G. *et al.* REV7 counteracts DNA double-strand break resection and affects PARP inhibition. *Nature* **521**, 541–544 (2015).
11. Boersma, V. *et al.* MAD2L2 controls DNA repair at telomeres and DNA breaks by inhibiting 5' end resection. *Nature* **521**, 537–40 (2015).
12. Bouwman, P. *et al.* 53BP1 loss rescues BRCA1 deficiency and is associated with triple-negative and BRCA-mutated breast cancers. *Nat. Struct. Mol. Biol.* **17**, 688–695 (2010).
13. Bunting, S. F. *et al.* 53BP1 Inhibits Homologous Recombination in Brca1-Deficient Cells by Blocking Resection of DNA Breaks. *Cell* **141**, 243–254 (2010).
14. Chapman, J. R. *et al.* RIF1 Is Essential for 53BP1-Dependent Nonhomologous End Joining and Suppression of DNA Double-Strand Break Resection. *Mol. Cell* **49**, 858–871 (2013).
15. Escobedo-Díaz, C. *et al.* A Cell Cycle-Dependent Regulatory Circuit Composed of 53BP1-RIF1 and BRCA1-CtIP Controls DNA Repair Pathway Choice. *Mol. Cell* **49**, 872–883 (2013).
16. Noordermeer, S. M. *et al.* The shieldin complex mediates 53BP1-dependent DNA repair. *Nature* **560**, 117–121 (2018).
17. Ghezraoui, H. *et al.* 53BP1 cooperation with the REV7–shieldin complex underpins DNA structure-specific NHEJ. *Nature* **560**, 122–127 (2018).
18. Dev, H. *et al.* Shieldin complex promotes DNA end-joining and counters homologous recombination in BRCA1-null cells. *Nat. Cell Biol.* **20**, 954–965 (2018).
19. Scully, R., Panday, A., Elango, R. & Willis, N. A. Stalled replication forks DNA double-strand break repair-pathway choice in somatic mammalian cells D N A D A m A g e. doi:10.1038/s41580-019-0152-0
20. Jaspers, J. E. *et al.* Loss of 53BP1 causes PARP inhibitor resistance in BRCA1-mutated mouse mammary tumors. *Cancer Discov.* **3**, 68–81 (2013).
21. Cruz, C. *et al.* RAD51 foci as a functional biomarker of homologous recombination repair and PARP inhibitor resistance in germline BRCA-mutated breast cancer. *Ann. Oncol.* **29**, 1203–1210 (2018).
22. Waks, A. G. *et al.* Reversion and non-reversion mechanisms of resistance to PARP inhibitor or platinum chemotherapy in BRCA1/2-mutant metastatic breast cancer. *Ann. Oncol.* **31**, 590–598 (2020).
23. Paes Dias, M. *et al.* Loss of nuclear DNA ligase III reverts PARP inhibitor resistance in BRCA1/53BP1 double-deficient cells by exposing ssDNA gaps. *Mol. Cell* (2021).
24. Tzelepis, K. *et al.* A CRISPR Dropout Screen Identifies Genetic Vulnerabilities and Therapeutic Targets in Acute Myeloid Leukemia. *Cell Rep.* **17**, 1193–1205 (2016).
25. King, M. P. & Attardi, G. Human cells lacking mtDNA: Repopulation with exogenous mitochondria by complementation. *Science (80-.)*. **246**, 500–503 (1989).
26. Juhász, S. *et al.* The chromatin remodeler ALC1 underlies resistance to PARP inhibitor treatment. *Sci. Adv.* **6**, 8626–8644 (2020).
27. Blessing, C. *et al.* The Oncogenic Helicase ALC1 Regulates PARP Inhibitor Potency by Trapping PARP2 at DNA Breaks. *Mol. Cell* **80**, 862–875.e6 (2020).
28. Verma, P. *et al.* ALC1 links chromatin accessibility to PARP inhibitor response in homologous recombination-deficient cells. *Nat. Cell Biol.* **23**, 160–171 (2021).
29. Hewitt, G. *et al.* Defective ALC1 nucleosome remodeling confers PARPi sensitization and synthetic lethality with HRD. *Mol. Cell* **81**, 767–783.e11 (2021).
30. Guo, K. *et al.* Ablation of Ggnbp2 impairs meiotic DNA double-strand break repair during spermatogenesis in

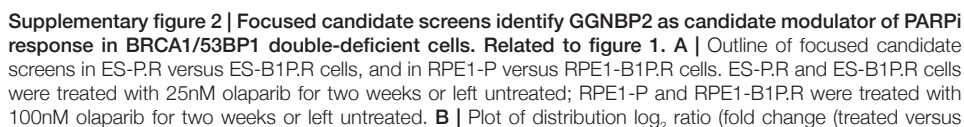
- mice. *J. Cell. Mol. Med.* **22**, 4863–4874 (2018).
31. Chen, A. *et al.* GGNBP2 is necessary for testis morphology and sperm development. *Sci. Reports* 2017 71 **7**, 1–8 (2017).
 32. Priestley, P. *et al.* Pan-cancer whole-genome analyses of metastatic solid tumours. *Nature* **575**, 210–216 (2019).
 33. Brinkman, E. K., Chen, T., Amendola, M. & van Steensel, B. Easy quantitative assessment of genome editing by sequence trace decomposition. *Nucleic Acids Res.* **42**, e168–e168 (2014).
 34. Birsoy, K. *et al.* An Essential Role of the Mitochondrial Electron Transport Chain in Cell Proliferation Is to Enable Aspartate Synthesis. *Cell* **162**, 540–551 (2015).
 35. Gui, D. Y. *et al.* Environment Dictates Dependence on Mitochondrial Complex I for NAD⁺ and Aspartate Production and Determines Cancer Cell Sensitivity to Metformin. *Cell Metab.* **24**, 716–727 (2016).
 36. Sullivan, L. B. *et al.* Supporting Aspartate Biosynthesis Is an Essential Function of Respiration in Proliferating Cells Article Supporting Aspartate Biosynthesis Is an Essential Function of Respiration in Proliferating Cells. *Cell* **162**, 552–563 (2015).
 37. Evers, B. *et al.* Selective Inhibition of BRCA2-Deficient Mammary Tumor Cell Growth by AZD2281 and Cisplatin. *Clin. Cancer Res.* **14**, 3916–3925 (2008).
 38. Abreu, C. M. *et al.* Shu complex SWS1-SWSAP1 promotes early steps in mouse meiotic recombination. *Nat. Commun.* **9**, 1–13 (2018).
 39. Liu, T., Wan, L., Wu, Y., Chen, J. & Huang, J. hSWS1•SWSAP1 is an evolutionarily conserved complex required for efficient homologous recombination repair. *J. Biol. Chem.* **286**, 41758–41766 (2011).
 40. Martino, J. *et al.* The human Shu complex functions with PDS5B and SPIDR to promote homologous recombination. *Nucleic Acids Res.* **47**, 10151 (2019).
 41. Prakash, R. *et al.* Distinct pathways of homologous recombination controlled by the SWS1-SWSAP1-SPIDR complex. *Nat. Commun.* **12**, (2021).
 42. Barazas, M. *et al.* Radiosensitivity Is an Acquired Vulnerability of PARPi-Resistant BRCA1-Deficient Tumors. *Cancer Res.* **79**, 452–460 (2019).
 43. Rein, H. L., Bernstein, K. A. & Baldock, R. A. RAD51 paralog function in replicative DNA damage and tolerance. *Curr. Opin. Genet. Dev.* **71**, 86–91 (2021).
 44. Ray Chaudhuri, A. *et al.* Replication fork stability confers chemoresistance in BRCA-deficient cells. *Nature* **535**, 382–387 (2016).
 45. Pulver, E. M. *et al.* A BRCA1 Coiled-Coil Domain Variant Disrupting PALB2 Interaction Promotes the Development of Mammary Tumors and Confers a Targetable Defect in Homologous Recombination Repair. *Cancer Res.* **81**, 6171–6182 (2021).
 46. Gogola, E. *et al.* Selective Loss of PARG Restores PARylation and Counteracts PARP Inhibitor-Mediated Synthetic Lethality. *Cancer Cell* **33**, 1078–1093.e12 (2018).
 47. Knijnenburg, T. A. *et al.* Genomic and Molecular Landscape of DNA Damage Repair Deficiency across The Cancer Genome Atlas. *Cell Rep.* **23**, 239–254.e6 (2018).
 48. Paes Dias, M., Rottenberg, S. & Jonkers, J. Functional genetic dropout screens and in vivo validation of candidate therapeutic targets using mouse mammary tumoroids. *STAR Protoc.* **3**, 101132 (2022).
 49. Bajrami, I. *et al.* Synthetic lethality of PARP and NAMPT inhibition in triple-negative breast cancer cells. *EMBO Mol. Med.* **4**, 1087–1096 (2012).
 50. Bian, C. *et al.* NADP⁺ is an endogenous PARP inhibitor in DNA damage response and tumor suppression. *Nat. Commun.* **10**, 693 (2019).
 51. Lahiguera, Á. *et al.* Tumors defective in homologous recombination rely on oxidative metabolism: relevance to treatments with PARP inhibitors. *EMBO Mol. Med.* **12**, e11217 (2020).
 52. Prakash, R., Zhang, Y., Feng, W. & Jasin, M. Homologous recombination and human health: The roles of BRCA1, BRCA2, and associated proteins. *Cold Spring Harb. Perspect. Biol.* **7**, (2015).
 53. Couturier, A. M. *et al.* Roles for APRIN (PDS5B) in homologous recombination and in ovarian cancer prediction. *Nucleic Acids Res.* **44**, 10879–10897 (2016).
 54. Bonilla, B. *et al.* The Shu complex prevents mutagenesis and cytotoxicity of single-strand specific alkylation lesions. *Elife* **10**, (2021).
 55. Godin, S. K. *et al.* The Shu complex promotes error-free tolerance of alkylation-induced base excision repair products. *Nucleic Acids Res.* **44**, 8199–8215 (2016).
 56. Bernstein, K. A., Juanchich, A., Sunjevaric, I. & Rothstein, R. The Shu complex regulates Rad52 localization during rDNA repair. *DNA Repair (Amst)*. **12**, 786–790 (2013).
 57. Jaspers, J. E. *et al.* Loss of 53BP1 Causes PARP Inhibitor Resistance in Brca1 -Mutated Mouse Mammary Tumors. *Cancer Discov.* **3**, 68–81 (2013).
 58. Love, M. I., Huber, W. & Anders, S. Moderated estimation of fold change and dispersion for RNA-seq data with DESeq2. *Genome Biol.* **15**, 550 (2014).
 59. Li, W. *et al.* MAGeCK enables robust identification of essential genes from genome-scale CRISPR/Cas9 knockout screens. *Genome Biol.* **15**, 554 (2014).
 60. Joung, J. *et al.* Genome-scale CRISPR-Cas9 knockout and transcriptional activation screening. *Nat. Protoc.* **12**,

- 828–863 (2017).
61. Ray Chaudhuri, A. *et al.* Topoisomerase α poisoning results in PARP-mediated replication fork reversal. *Nat. Struct. Mol. Biol.* **19**, 417–423 (2012).
62. Cameron, D. L. *et al.* Gridss, purple, linx: Unscrambling the tumor genome via integrated analysis of structural variation and copy number. *bioRxiv* 781013 (2019).

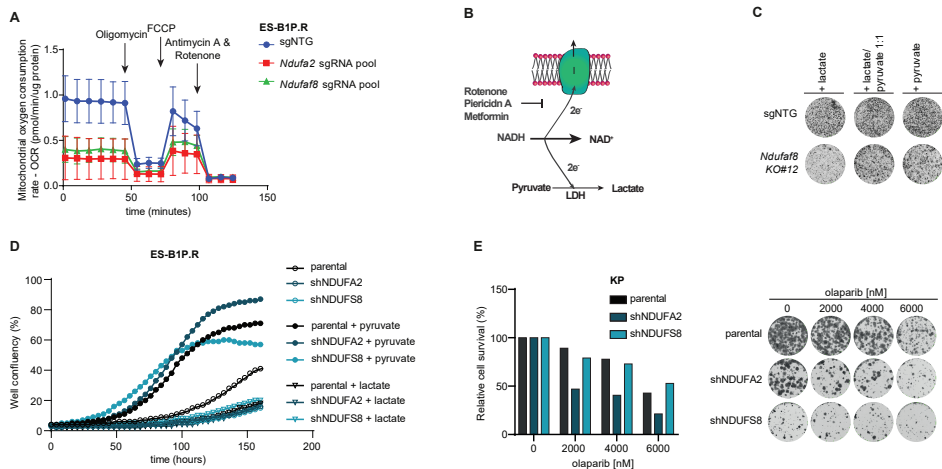
SUPPLEMENTARY FILES



Supplementary figure 1 | STRING and KEGG pathway analysis of all genes included in the focused screen library (FDRs3). Related to figure 1. A | Genome-wide screen hit selection criteria. B-C | STRING network (<https://string-db.org/>) (B) and KEGG pathway (C) analysis of genes included in the focused library.

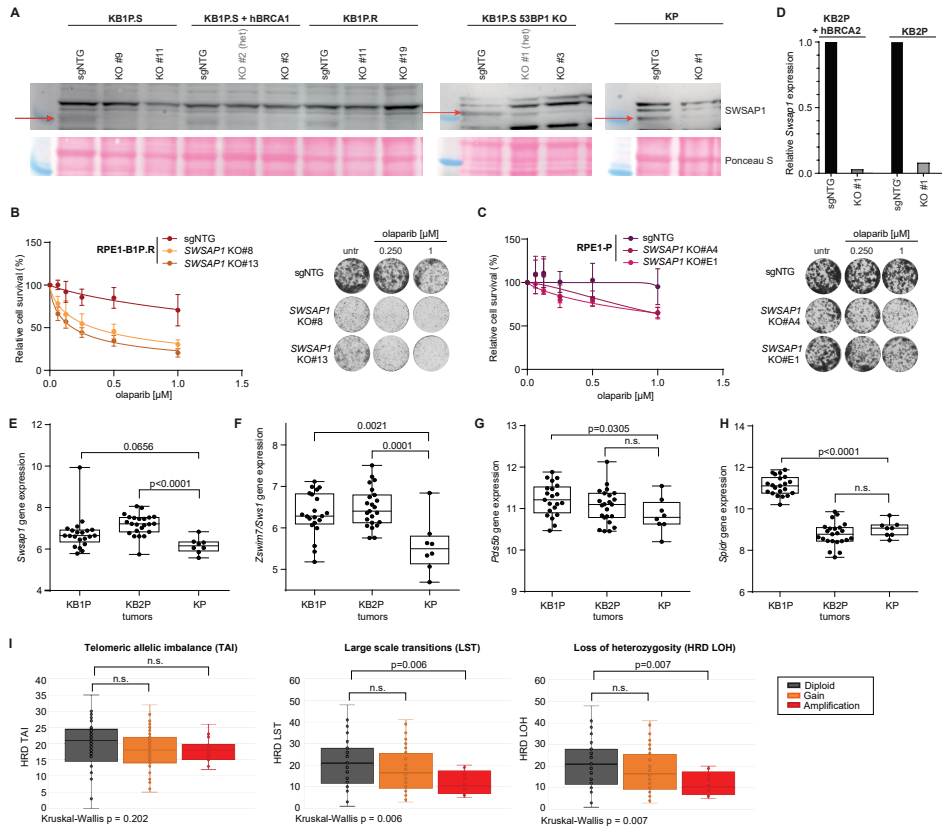


untreated)) median for all genes versus false discovery rate (FDR) of results from screen using focused candidate library in ES-P.R cells. **C** | Plot of distribution \log_2 ratio (fold change (treated versus untreated)) median for all genes versus FDR of results from screen using focused candidate library in RPE1-P cells. **D** | Plot of distribution \log_2 ratio (fold change (untreated versus T0)) median for all genes versus FDR of results from screen using focused candidate library in ES-B1P.R cells. **E** | Plot of distribution \log_2 ratio (fold change (untreated versus T0)) median for all genes versus FDR of results from screen using focused candidate library in ES-P.R cells. **F** | Plot of distribution \log_2 ratio (fold change (untreated ES-B1P.R versus untreated ES-P.R)) median for all genes versus false FDR of results from screen using focused candidate library in mES cells. **G** | Quantification and representative images of long-term clonogenic assays in *Trp53bp1*-deleted KB1P.S (KB1P.S-53BP1KO) cells; treated with olaparib. Cells were treated for the whole extent of the assay. **H** | Relative *Ggnbp2* expression quantified by RT-PCR. **I** | Correlation between *GGNBP2* copy number aberrations and PARPi response in patients. Y-axis indicates *GGNBP2* copy number status of metastatic solid tumors prior to PARPi (olaparib or niraparib) treatment. The description of the tumor types corresponds to the primary tumor location. First treatment response was evaluated according to RECIST (response was measured every 8 to 12 weeks) and categorized into PD, Progressive disease; SD, stable disease; or PR, partial response. PARPi was given as single agent or combination with other drugs. Data was obtained from the Hartwig Medical Foundation.



Supplementary figure 3 | Effect of pyruvate supplementation in MCI-deficient cells. Related to figure 2.

A | Mito stress test assay used to quantify mitochondrial oxygen consumption rate (OCR) with the Seahorse Bioanalyzer XFe24 in ES-B1P.R transduced with sgRNA non-targeting (sgNTG) or with sgRNA targeting the genes *Ndufa2* and *Ndufa8*. **B** | Schematic illustration of how oxygen allows cells to regenerate NAD⁺ from NADH via MCI activity and the MCI inhibitors used in this study. Exogenous pyruvate provides an alternate way to regenerate NAD⁺ through lactate dehydrogenase (LDH) activity. Adapted from Gui et al.³⁵. **C** | Representative images of ES-B1P.R cells cultured for 10 days in medium supplemented with 1 mM lactate and/or 1 mM pyruvate. **D** | Quantification of proliferation assays in ES-B1P.R cells. Media was supplemented with 1 mM pyruvate or 1 mM lactate, as indicated. Cell confluency was measured every 4h with IncuCyte. **E** | Quantification and representative images of long-term clonogenic assays in KP cells, treated with olaparib. Cells were treated for the whole extent of the assay.




Supplementary figure 4 | BRCA1/2-deficient cells may display increased dependency on the Shu complex. Related to figure 3 and 5. A | Western blot analysis of SWSAP1 in mouse tumor cells. **B-C |** Quantification and representative images of long-term clonogenic assays in RPE1-B1P.R (E) and RPE1-P (F) cells treated with olaparib. Cells were treated for the whole extent of the assay. **D |** Relative *Swsap1* gene expression in the indicated cells quantified by RT-PCR. **E-H |** Gene expression of Shu complex factors *Swsap1* (E), *Zswim7* (F), *Pds5b* (G) and *Spidr* (H), in KB1P, KB2P and KP naïve tumors, measured by RNA-seq. Statistical analysis was carried out using unpaired t test. **I |** Association between SWSAP1 amplification and HRD sub scores: telomeric allelic imbalance (TAI), large-scale transition (LST), and loss-of-heterozygosity (HRD LOH).

Supplementary Table 1 | Log₂ fold change (treated versus untreated) of each sgRNA scoring as hit. Related to figure 1.

log₂(fold change)

0 2 4 6



	treated vs T0	untreated vs T0	treated vs untreated
<i>Ndufa8-4</i>	-4.23	1.08	-5.31
<i>Ndufa8-1</i>	-4.24	0.64	-4.88
<i>Ndufa8-3</i>	-3.02	0.75	-3.77
<i>Ndufa2-5</i>	-3.26	0.67	-3.94
<i>Ndufa2-1</i>	-3.33	0.28	-3.61
<i>Ndufa2-4</i>	-3.32	-0.11	-3.21
<i>Ndufb8-1</i>	-3.9	0.67	-4.57
<i>Ndufb8-5</i>	-3.58	0.51	-4.09
<i>Ndufb8-2</i>	-3.26	0.77	-4.03
<i>Ndufb8-3</i>	-3.32	0.48	-3.81
<i>Ndufs8-2</i>	-3.18	0.99	-4.18
<i>Ndufs8-1</i>	-3	0.54	-3.54
<i>Ndufa1-3</i>	-3.69	0.28	-3.97
<i>Ndufa1-1</i>	-3.66	0.26	-3.92
<i>Ndufs7-5</i>	-4.34	0.81	-5.15
<i>Ndufs7-2</i>	-4.57	0.53	-5.1
<i>Ndufs7-3</i>	-4.27	0.55	-4.81
<i>Ndufs7-4</i>	-3.04	0.57	-3.61
<i>Ndufs1-1</i>	-4.27	0.38	-4.65
<i>Ndufs1-2</i>	-4.08	0.08	-4.16
<i>Ndufs1-4</i>	-3.07	0.8	-3.87
<i>Ndufb4-1</i>	-3.47	0.84	-4.31
<i>Ndufb4-3</i>	-3.02	0.86	-3.88
<i>Ndufb4-2</i>	-3.43	-0.1	-3.34
<i>Ndufa3-3</i>	-3.32	0.6	-3.92
<i>Ndufa3-5</i>	-3.04	0.57	-3.61
<i>Zswim7-5</i>	-7.59	-0.82	-6.77
<i>Zswim7-4</i>	-6.49	-1.02	-5.47
<i>Zswim7-2</i>	-5.72	-1.34	-4.38
<i>Zswim7-1</i>	-4.94	-0.77	-4.17
<i>Polb-2</i>	-7.22	0.26	-7.49
<i>Polb-5</i>	-3.86	0.16	-4.02
<i>Swsap1-5</i>	-5.36	-0.56	-4.8
<i>Swsap1-4</i>	-5.71	-1.34	-4.37
<i>Swsap1-2</i>	-4.44	-0.57	-3.88
<i>Ndufb7-3</i>	-4.06	0.44	-4.49
<i>Ndufb7-5</i>	-3.51	0.66	-4.18
<i>Nubpl-2</i>	-3.42	1.01	-4.43
<i>Nubpl-4</i>	-3.32	0.85	-4.17
<i>Ndufb10-2</i>	-4.16	0.27	-4.43
<i>Ndufb10-1</i>	-3.14	0.65	-3.79
<i>Cops7a-2</i>	-6.5	-1.19	-5.31
<i>Cops7a-4</i>	-5.03	-0.5	-4.54
<i>Ndufaf5-3</i>	-4.05	0.46	-4.51
<i>Ndufaf5-5</i>	-3.08	0.53	-3.6
<i>Ndufaf5-1</i>	-3	0.42	-3.42

Supplementary Table 2 | genes included in focused candidate library (FDR≤0.3). Related to figure 1.

Gene	FDR	Gene	FDR	Gene	FDR	Gene	FDR	Gene	FDR	Gene	FDR	Gene	FDR
Ndufa8	0.000075	Ndufa2	0.000075	Cox6b1	0.000193	Oxsl	0.004624	Dusp11	0.031564	Fasickd5	0.082668	Seld2	0.137277
3110001D03Rik	0.000075	Ndufa3	0.000075	Lprt1	0.000193	Pob	0.005321	Spdr	0.032875	Hsd1d0	0.084774	Hs2bp	0.142774
Adck4	0.000075	Ndufa8	0.000075	Ndufa11	0.000193	Ndufa11	0.005638	Hngcs1	0.035	Rads1b	0.092029	Mnos1	0.142774
Atpsl	0.000075	Ndufa5	0.000075	Ndufa3	0.000193	2810006K23Rik	0.005768	Siva1	0.036544	Ddx17	0.09521	Wash	0.146872
Cars2	0.000075	Ndufa6	0.000075	Ndufa2	0.000193	Ptpn2	0.006616	Cand1	0.036634	Agc2	0.095427	Mps18a	0.153235
Ccdc101	0.000075	Ndufa7	0.000075	Rad54l	0.000193	4930432K21Rik	0.006703	Wtsc1	0.042011	Prr12	0.095427	Tgfr1	0.156468
Chc1	0.000075	Ndufb10	0.000075	Srsf6	0.000193	Ints12	0.006703	Rrfb	0.043183	Polidp2	0.098275	Tic7b	0.162773
Clpp	0.000075	Ndufb4	0.000075	Ndufb2	0.000254	Mtrf11	0.006703	Smacal1	0.043183	Dnajb6	0.098768	Pds5b	0.164343
Cjpx	0.000075	Ndufb6	0.000075	Cox3	0.000306	Xrcc6bp1	0.006731	Tmem70	0.045552	Tsc2d2d	0.098768	Pced1a	0.166531
Coa4	0.000075	Ndufb8	0.000075	Hmnmpr	0.000306	Fdx1	0.007017	Cenpf	0.048614	Coa5	0.10074	Pds2	0.17401
Cops7a	0.000075	Ndufb9	0.000075	Prkar1a	0.000306	Mpl63	0.007468	Ankrd11	0.050026	Ndufa5	0.10074	Yap1	0.176359
Coq4	0.000075	Ndufc2	0.000075	Mnd1	0.000362	Cdk2	0.00952	Ogfd3	0.050026	Helq	0.102954	Sos2	0.17717
Coq5	0.000075	Ndufs1	0.000075	Msh2	0.000413	Ndufs5	0.009607	Iba57	0.051414	Mtg1	0.103122	Mtmt	0.183986
Coq6	0.000075	Ndufs2	0.000075	Ndufa3	0.000413	Arpp19	0.010442	Ube2f	0.052044	Ndufa2	0.103122	Sulf1c1	0.183986
Cox18	0.000075	Ndufs6	0.000075	Ndufa9	0.000524	Cks1b	0.010685	Ten1	0.053561	Khsrp	0.105775	Cnga1	0.185687
Cox41	0.000075	Ndufs7	0.000075	Uqcq	0.000633	Garn1	0.012151	Ngn	0.053789	Mtpap	0.105775	Gli1	0.185687
Cox5a	0.000075	Ndufs8	0.000075	Nubpl	0.001309	Ube2v1	0.013594	Pgfr1	0.053825	Chd1l	0.1061	Atm	0.193331
Cpx	0.000075	Ndufv1	0.000075	Ndufb7	0.001406	Trifsf8	0.013725	Oxsm	0.054144	Sic25a32	0.10632	Six4	0.198085
Ddx5	0.000075	Pds1	0.000075	Coq7	0.001502	Sp2	0.013774	Sm3a	0.054144	Rprd1b	0.106946	Lphn1	0.204311
Dhx30	0.000075	Ppx	0.000075	Coa6	0.001776	Ndufb5	0.014535	Bre	0.055255	Pcdha9	0.108403	Bst1l	0.20579
Ecsit	0.000075	Psmc3ip	0.000075	Lip2	0.001776	Bcof1	0.015362	Tralp	0.055255	4930427A07Rik	0.108441	Cttn1	0.212957
Foxed1	0.000075	Rth4ip1	0.000075	Uqcq	0.001776	Plecxl1	0.016489	Nbp1	0.055831	Coq3	0.111489	Axnm73	0.213021
Gfm2	0.000075	Selc1	0.000075	Sp1	0.001863	Uqcrl1	0.017597	Lhx1	0.058768	Zkscan17	0.113836	Baz1b	0.216271
Gtpbp3	0.000075	Sic25a51	0.000075	Gnbp2	0.002159	Tmem126b	0.018966	Ptdc1	0.061489	Ahsa1	0.116051	Ssh1	0.221186
Higd2a	0.000075	Swi5	0.000075	Ndufa1	0.002241	Cyc1	0.020373	Prc2b	0.063156	Sic25a3	0.116906	Cik1	0.222351
Hmbs	0.000075	Swap1	0.000075	Ndufc1	0.002424	Mecr	0.025982	H2afx	0.063561	Tlk2	0.121989	1200014J11Rik	0.223381
Kmt2b	0.000075	Tmmdc1	0.000075	Ndufa4	0.002501	Igf2bp1	0.026365	Torg4	0.063561	Eme1	0.127512	Zbb44	0.228329
Lin28a	0.000075	Ttr1	0.000075	Sic25a19	0.00298	Lias	0.026614	Ybe1	0.063561	Tmt1	0.128445	Scnm1	0.231779
Mcat	0.000075	Uros	0.000075	Gtpbp8	0.003317	Cox6a1	0.029226	Zfp933	0.064825	Lym2	0.12864	2310003H01R-ik	0.24042
Mn1	0.000075	Usp22	0.000075	Uqcrl	0.003317	Uba6	0.029226	Hmnpab	0.065609	C1qbp	0.130621	Scaf11	0.244823
Mrrf	0.000075	Zswim7	0.000075	Hat1	0.003382	Topors	0.029233	Mif3	0.071912	Znrf3	0.131092	Mterf3	0.245491
Mto1	0.000075	Coq2	0.000148	Cabin1	0.003446	Ube2cbp	0.029233	Tars2	0.075322	Ahdct1	0.132021	Rnaaseh2a	0.245956
Ndufa1	0.000075	Abhd11	0.000193	Ndufb3	0.003605	Pph1	0.030313	Nsun4	0.078753	Dnajc6	0.132021	Sub1	0.245956
Ndufa10	0.000075	Acard9	0.000193	Ndufs4	0.003913	Morc2a	0.030807	Tnrc6c	0.078753	Dscr3	0.133142	Gsch	0.249209
Ndufa13	0.000075	Bola3	0.000193	Prc2a	0.003913	Rfox13	0.030941	Scd2	0.079802	Pmk1	0.137129	Zmym4	0.249768